



Global Biogeochemical Cycles^a



RESEARCH ARTICLE

10.1029/2021GB007131

Key Points:

- A new, dynamic marine particle cycling model reproduces the observed attenuation of sinking particulate organic carbon fluxes at 22 locations
- Particle properties, ocean temperature, and to a lesser extent, seawater viscosity explain most of the large-scale differences in mesopelagic carbon transfer efficiency
- Particles transport organic carbon downward more efficiently at high latitudes than at low latitudes, consistent with recent studies

Correspondence to:

A. Dinauer, ashdinauer@gmail.com

Citation:

Dinauer, A., Laufkötter, C., Doney, S. C., & Joos, F. (2022). What controls the large-scale efficiency of carbon transfer through the ocean's mesopelagic zone? Insights from a new, mechanistic model (MSPACMAM). Global Biogeochemical Cycles, 36, e2021GB007131. https://doi.org/10.1029/2021GB007131

Received 22 JUL 2021 Accepted 26 JUL 2022

© 2022. The Authors.

This is an open access article under the terms of the Creative Commons Attribution-NonCommercial-NoDerivs License, which permits use and distribution in any medium, provided the original work is properly cited, the use is non-commercial and no modifications or adaptations are made.

What Controls the Large-Scale Efficiency of Carbon Transfer Through the Ocean's Mesopelagic Zone? Insights From a New, Mechanistic Model (MSPACMAM)

Ashley Dinauer¹, Charlotte Laufkötter¹, Scott C. Doney², and Fortunat Joos¹

¹Climate and Environmental Physics, Physics Institute and Oeschger Centre for Climate Change Research, University of Bern, Switzerland, ²Department of Environmental Sciences, University of Virginia, Charlottesville, VA, USA

Abstract A key challenge for current-generation Earth system models (ESMs) is the simulation of the penetration of sinking particulate organic carbon (POC) into the ocean interior, which has implications for projections of future oceanic carbon sequestration in a warming climate. This paper presents a new, cost-efficient, mechanistic 1D model that prognostically calculates POC fluxes by carrying four component particles in two different size classes. Gravitational settling and removal/transformation processes are represented explicitly through parameterizations that incorporate the effects of particle size and density, dissolved oxygen, calcite and aragonite saturation states, and seawater temperature, density, and viscosity. The model reproduces the observed POC flux attenuation at 22 locations in the North Atlantic and North Pacific. The model is applied over a global ocean domain with seawater properties prescribed from observation-based climatologies in order to address an important scientific question: What controls the spatial pattern of mesopelagic POC transfer efficiency? The simulated vertical POC transfer is more efficient at high latitudes than at low latitudes with the exception of oxygen minimum zones, which is consistent with recent inverse modeling and neutrally buoyant sediment trap studies. Here, model experiments show that the relative abundance of large-sized, rapidly sinking particles and the slower rate of remineralization at high latitudes compensate for the region's lack of calcium carbonate ballast and the cold-water viscous resistance, leading to higher transfer efficiencies compared to low-latitude regions. The model could be deployed in ESMs in order to diagnose the impacts of climate change on oceanic carbon sequestration and vice versa.

1. Introduction

The ocean's "biological pump" refers to the physical and biogeochemical processes that transport organic carbon in the particulate (POC) and dissolved (DOC) forms, along with biogenic calcium carbonate (CaCO₃), into the ocean interior where they are converted to their dissolved, inorganic forms. The net effect of these processes is to create and maintain vertical concentration gradients of dissolved inorganic carbon (DIC), alkalinity, and nutrients (Volk & Hoffert, 1985). The amount of organic carbon exported from the surface euphotic zone (100 m), usually referred to as carbon export, is dominated by the POC component with DOC contributing only about 20% to the total flux (Hansell et al., 2009). Estimates of global carbon export range from 5 to 12 Pg C yr⁻¹ (DeVries & Weber, 2017; Dunne et al., 2007; Henson et al., 2011; Laws et al., 2000; Siegel et al., 2014). The major pathway for vertical POC transport is the gravitational settling of particles, although diel (or seasonal) vertically migrating zooplankton can also play a role in transporting POC to depth (Archibald et al., 2019; Boyd et al., 2019; Ducklow et al., 2001; Siegel et al., 2016). Below the well-lit surface ocean, the downward rain of POC is consumed and respired by heterotrophic bacteria, detritivorous zooplankton, and larger animals in the mesopelagic zone (100–1,000 m) (Giering et al., 2014; Steinberg et al., 2008). Physical circulation and vertical mixing processes return DIC- and nutrient-rich waters at depth to the surface euphotic zone on multi-decadal to millennial timescales with this nutrient supply supporting primary production.

The vertical transport of POC into the ocean interior has important implications for the air-sea carbon dioxide (CO_2) balance (Kwon et al., 2009; Matsumoto, 2007; Matsumoto et al., 2007; Roth et al., 2014; Segschneider & Bendtsen, 2013). An increase of only ~25 m in the global mean penetration depth of POC has the effect of lowering atmospheric CO_2 concentrations by 10–27 ppm on the millennial timescale during which the ocean reaches a new equilibrium (Kwon et al., 2009), which are expected to decrease further on multi-millennial timescales due to the exchange fluxes between the ocean, marine sediments and lithosphere (Roth et al., 2014). The deeper

DINAUER ET AL. 1 of 34

the penetration of POC, the longer the timescale of oceanic carbon sequestration and the greater the atmospheric CO_2 drawdown. The fraction of sinking POC that is released as DIC in deep waters below the base of the mesopelagic zone (1,000 m) is returned to the surface ocean on centennial to millennial timescales by the deep ocean's overturning circulation (Primeau, 2005). Thus, a reasonable way to quantify the efficiency of vertical POC penetration is to calculate the fraction of POC export that reaches 1,000 m, referred to here as mesopelagic transfer efficiency ($T_{\rm eff}$).

Initial field studies by Martin et al. (1987) suggested that $T_{\rm eff}$ is about 14%. However, their observational coverage was limited to the North Pacific, and the generality of their measured $T_{\rm eff}$ was unclear. Further field studies have demonstrated that $T_{\rm eff}$ varies regionally, although there is disagreement over the latitudinal pattern. Combined analyses of deep-sea sediment trap data and 234 Th-based surface export estimates (Francois et al., 2002; Henson et al., 2012; Lutz et al., 2002) suggest that $T_{\rm eff}$ is higher in low-latitude regions, whereas the flux measurements collected by free-drifting neutrally buoyant sediment traps (NBSTs) (Buesseler et al., 2007; Marsay et al., 2015) indicate that $T_{\rm eff}$ is higher in high-latitude regions. Some global ocean biogeochemical models simulate a spatial pattern of $T_{\rm eff}$ that is consistent with the findings of deep-sea sediment trap studies (e.g., Lima et al., 2014), and some support the conclusions drawn by NBST studies (e.g., DeVries & Weber, 2017; Maerz et al., 2020). Recent inverse modeling studies (Weber et al., 2016) and 1D particle flux models (Cram et al., 2018) report strong latitudinal gradients in $T_{\rm eff}$ ranging from roughly 5% at low latitudes to 35% at high latitudes.

Predicting the response of the biological pump to changing climate/ocean conditions requires a mechanistic understanding of global T_{eff} variability. Although some progress has been made (Cram et al., 2018), the underlying processes that control the large-scale pattern of $T_{\rm eff}$ are not well established. $T_{\rm eff}$ at any one site reflects the balance between the rate at which particles sink and the rate at which organic carbon is lost from the sinking particles (Kwon et al., 2009; McDonnell et al., 2015; Omand et al., 2020). Observed rates of gravitational settling of particles vary considerably in space and time (McDonnell & Buesseler, 2010) from <10 to typically hundreds of meters per day (Turner, 2002, 2015). The settling velocity of a particle depends primarily on its size, density, and other properties (e.g., shape and fractal dimension) as well as the density and viscosity of the fluid through which it moves (Alldredge & Gotschalk, 1988; Laurenceau-Cornec et al., 2015; Rubey, 1933; Taucher et al., 2014). The properties of the particles settling out of the surface ocean are determined by the species composition of the phytoplankton community (Boyd & Newton, 1999; Guidi et al., 2009; Weber et al., 2016) and the aggregation processes (e.g., physical coagulation and fecal pellet production) that formed them (Burd & Jackson, 2009). Several studies have highlighted the potential importance of ballast minerals, such as CaCO₃ and opal, in increasing particle density and thus sinking speed (Armstrong et al., 2002; Klaas & Archer, 2002; Iversen & Ploug, 2010; Ploug, Iversen, & Fischer, 2008, Ploug, Iversen, Koski, & Buitenhuis, 2008). Particle properties are altered further in the water column by particle transformation processes, such as bacterial solubilization, consumption and repackaging by zooplankton, particle disaggregation (or fragmentation), and mineral dissolution (Boyd & Stevens, 2002; Boyd & Trull, 2007; Boyd et al., 1999; Briggs et al., 2020; Buesseler & Boyd, 2009; Collins et al., 2015; Stemmann et al., 2004).

Remineralization and fragmentation processes are important for transforming POC into its suspended or dissolved forms. Particle-attached bacteria solubilize POC into DOC, which is subsequently converted to DIC during respiration by either attached or free-living bacteria. Several factors, including temperature (Iversen & Ploug, 2013; Marsay et al., 2015), dissolved oxygen (Devol & Hartnett, 2001; Laufkötter et al., 2017; Van Mooy et al., 2002; Weber & Bianchi, 2020), and lability of POC (Aumont et al., 2017; Francois et al., 2002; Henson et al., 2012), are thought to determine the rate of bacterial respiration. It is uncertain whether ballast minerals provide physical protection against bacterial activity for labile POC (Iversen & Ploug, 2010; Ploug, Iversen, & Fischer, 2008, Ploug, Iversen, Koski, & Buitenhuis, 2008). There is an increasing appreciation of the important role that physically and/or biologically mediated fragmentation plays in modulating the sinking POC flux (Briggs et al., 2020; Cavan et al., 2017). Zooplankton "sloppy feeding" (Anderson & Tang, 2010; Lampitt et al., 1990) and swimming behavior (Dilling & Alldredge, 2000; Goldthwait et al., 2004), along with turbulence-generated shear stress (Alldredge et al., 1990), potentially fragment large particles into smaller, slowly sinking or nonsinking (suspended) ones.

The complexity of transport and transformation processes makes model representation of marine particle fluxes challenging. Historically, Earth system models (ESMs) have adopted an empirical approach to the parameterization of sinking POC fluxes (Najjar et al., 2007). The most common approach is to calculate the POC flux at

DINAUER ET AL. 2 of 34

depth z, F(z), using the power-law "Martin curve," i.e., $F(z) = F_{100}(z/100)^{-b}$, where F_{100} is the POC export flux at 100 m and b is the attenuation coefficient (Martin et al., 1987). This approach has some important limitations. It has become clear that the value of b cannot be uniformly applied (Henson et al., 2012; Marsay et al., 2015). It is also clear that the POC flux attenuation predicted by a power law does not hold for oxygen minimum zones (Weber & Bianchi, 2020). Importantly, ESMs that employ an empirical flux-vs.-depth relationship are limited in their ability to simulate the past or future response of flux attenuation to changing climate/ocean conditions.

Marine ecosystem models have seen a number of improvements in the representation of the biological pump, with the caveat that they tend to focus on surface-ocean food web processes rather than the details of particle sinking and transformations in the mesopelagic zone. Many ecosystem models now include some formulation of temperature and/or oxygen effects on microbial remineralization along with implicit or explicit parameterizations of zooplankton grazing (e.g., Aumont et al., 2015; DeVries & Weber, 2017; Keller et al., 2012; Quéré et al., 2016; Yool et al., 2013). However, particle settling velocities are either prescribed as a fixed value or calculated as a function of depth, while fragmentation processes are either parameterized in an implicit fashion or neglected altogether. More complex 1D models have been developed to provide insight into the mesopelagic food web structure and associated particle transformations (e.g., Anderson & Tang, 2010; Boyd & Stevens, 2002; Dadou et al., 2001; Giering et al., 2014; Jackson & Burd, 2002; Stemmann et al., 2004), yet these models are often designed and evaluated for a single site. In addition, most particle transformation models have focused on the role of physical aggregation in determining the particle size spectrum (Burd, 2013; Burd and Jackson, 2002, 2009; Jackson, 1995; Jackson & Burd, 2015). A mechanistic marine aggregate sinking scheme has recently been developed and deployed in an ESM (Maerz et al., 2020), but a thorough examination of parameter uncertainties remains difficult owing to higher computational costs inherent in higher model complexity. The added complexity of aggregate dynamics can also introduce new sources of model errors and uncertainties by increasing the number of potentially poorly known input parameters. There is still a need for computationally efficient, dynamic marine particle cycling models that (a) are suitable for implementation in the ESMs used in climate research and (b) provide a viable tool for identifying the main drivers of global $T_{\rm eff}$ variability.

The broad objectives of this paper are to (a) provide a modeling framework that enables the simulation of $T_{\rm eff}$ on a global scale, (b) explore the range of model behavior in response to variations in the input parameters believed to be especially important for controlling $T_{\rm eff}$, and (c) determine the relative importance of various environmental factors in the spatial pattern of $T_{\rm eff}$. To achieve these goals, a new, dynamic 1D marine particle cycling model has been developed and implemented on a latitude–longitude–depth grid. The model performs well against a compilation of 27 field-derived sinking POC flux and oxygen consumption rate profiles. Our modeling approach has a number of advantages. First, POC fluxes are calculated interactively with reasonably sophisticated treatments of particle sinking and transformation processes, thereby requiring a relatively small number of input parameters. Second, the model's ocean state variables, including temperature, dissolved oxygen, density, viscosity, and calcite and aragonite saturation states, are prescribed using observation-based climatologies, which avoids some of the uncertainties and biases inherent in standard ocean circulation models (e.g., model deficiencies in the volume of oxygen minimum zones). Third, the computational efficiency of the model allows for an extensive assessment of parameter uncertainties.

2. Methods

2.1. Global Ocean Particle Cycling Model

The Model of Sinking Particles and Cycling of Marine Aggregated Matter (MSPACMAM) is a computationally efficient 1D marine particle cycling model that is well suited for implementation in ESMs. The model includes two representative size classes of biogenic particles that are sufficiently large and/or dense to gravitationally settle through the water column. The small particle size class represents nano- and micro-sized sinking particles, whereas particles in the large size class may be marine snow, fecal pellets, and/or phytodetritus. The model implicitly assumes that pico-sized particles are either remineralized or repackaged into larger (\geq nano-sized) particles in the surface ocean. Nonsinking (suspended) particles are not resolved. We assume that the sinking particles consist of four explicit components: particulate organic matter (POM), two forms of CaCO $_3$ (calcite and aragonite), and opal (SiO $_2$). This assumption is important since the various component particles making up aggregated matter each have their own densities and thereby play a role in determining particle settling velocities. The model explicitly represents the respiratory decomposition of organic matter (POC), mineral (calcite, aragonite,

DINAUER ET AL. 3 of 34

9449224, 2022, 10, Downloaded from https://agupubs.onlinelibrary.wiley.com/doi/10.1029/2021GB007131, Wiley Online Library on [18/11/2024]. See the Terms and Condi

The sinking POC flux associated with each size class is equal to the POC concentration, [POC], multiplied by the particle sinking speed, w_{sink} . The bulk sinking POC flux, F_{POC} , on a grid cell face is diagnosed by

$$F_{\text{POC}} = w_{\text{sink}}^{S} \left[\text{POC}^{S} \right] + w_{\text{sink}}^{L} \left[\text{POC}^{L} \right], \tag{1}$$

where subscripts S and L refer to the small and large particle size classes, respectively.

2.1.1. Model Equations for a Grid Cell

The model carries four different particle tracers in small (S) and large (L) size classes: POC (POC^S, POC^L), calcite ($^{calc}CaCO_3^S$; $^{calc}CaCO_3^L$), aragonite ($^{arag}CaCO_3^S$; $^{arag}CaCO_3^L$), and opal (SiO_2^S ; SiO_2^L). The time evolution of the concentration (in mol m⁻³) of particle tracer C in size class X, C^X , in a grid cell within the ocean model domain (defined here as 100 m to the ocean bottom) is given by

$$\frac{\partial \left[C^{X}\right]}{\partial t} = -\frac{\partial \left(w_{sink}^{X}\left[C^{X}\right]\right)}{\partial z} - k_{C}\left[C^{X}\right] - k_{frag}^{X}\left[C^{L}\right]. \tag{2}$$

The first term on the right-hand side of the equation is the advective flux divergence where w_{sink}^X is the settling velocity of the small or large particle; the second term is the loss term due to remineralization or dissolution where k_C is the particle tracer C loss rate in units of time⁻¹; and the third term is the source/sink term due to large particle fragmentation where $k_{frag}^S = -k_{frag}^L$ is the fragmentation rate constant.

2.1.1.1. Surface Boundary Fluxes

The prescribed boundary fluxes used to force the model include POC, calcite, aragonite, and opal export fluxes applied to the surface boundary at 100 m. We assume opal and aragonite export each originate from large plankton (diatoms and pteropods, respectively) and thus enter the large particle size class, whereas the POC and calcite export fluxes are partitioned into small and large particles. For simplicity, we assume the fraction of POC or calcite export that enters the large particle size class, σ_L , is proportional to the fractional contribution of opal and aragonite to total particle export:

$$\sigma_L = \kappa_L \frac{\text{opal}_e + \text{arag}_e}{\text{POC}_e + \text{calc}_e + \text{arag}_e + \text{opal}_e},$$
(3)

where κ_L is the constant of proportionality, and POC_e, calc_e, arag_e, and opal_e are the prescribed POC, calcite, aragonite, and opal export fluxes, respectively (see Appendix A2 for more details of these fluxes). The proportionality constant κ_L used in this study is one. The remaining fraction of POC or calcite export, $(1 - \sigma_L)$, is routed to the small particle size class. The scientific rationale for this export partitioning scheme is discussed further in Section 3.4.

2.1.1.2. Particle Settling Velocities

The sinking speeds of small and large particles, w_{sink}^S and w_{sink}^L , are diagnosed separately at each time step using Rubey's (1933) equation, which, unlike Stokes' (1851) law, applies in both the laminar (viscous) and turbulent (inertial) regimes. Rubey's equation equates the effective weight of a spherical particle to two different forces: (a) the viscous resistance of the fluid through which it moves and (b) the momentum of the fluid that strikes the particle. For an arbitrary size class, the particle settling velocity w_{sink}^X (in cm s⁻¹) at a tracer grid cell face is given by

$$w_{sink}^{X} = \frac{\sqrt{\frac{4}{3}g\rho_{sw}\left(\rho_{ptcl}^{X} - \rho_{sw}\right)r_{X}^{3} + 9\mu^{2}} - 3\mu}{\rho_{sw}r_{X}},$$
(4)

where g = 981 cm s⁻² is the acceleration due to gravity, ρ_{sw} is the in situ density of seawater (in g cm⁻³), ρ_{ptcl}^{X} is the bulk density of the small or large particle (in g cm⁻³), r_X is the prescribed effective radius of the small or large particle (in cm) (see Tables 1 and 2), and μ is the dynamic viscosity of seawater (in g cm⁻¹ s⁻¹).

DINAUER ET AL. 4 of 34

9449224, 2022, 10, Downloaded from https://agupubs. online library. wiley.com/doi/10.1029/2021GB007131, Wiley Online Library on [18/11/2024]. See the Terms and Conditions (https://onlinelibrary.wiley.com/terms-and-conditions) on Wiley Online Library for rules of use; OA articles are governed by the applicable Creative Creative Conditions (https://onlinelibrary.wiley.com/terms-and-conditions) on Wiley Online Library for rules of use; OA articles are governed by the applicable Creative Creative Conditions (https://onlinelibrary.wiley.com/terms-and-conditions) on Wiley Online Library for rules of use; OA articles are governed by the applicable Creative Creative Conditions (https://onlinelibrary.wiley.com/terms-and-conditions) on Wiley Online Library for rules of use; OA articles are governed by the applicable Creative Conditions (https://onlinelibrary.wiley.com/terms-and-conditions) on Wiley Online Library for rules of use; OA articles are governed by the applicable Creative Conditions (https://onlinelibrary.wiley.com/terms-and-conditions) on Wiley Online Library for rules of use; OA articles are governed by the applicable Creative Conditions (https://onlinelibrary.wiley.com/terms-and-conditions) on Wiley Online Library for rules of use; OA articles are governed by the applicable Creative Conditions (https://onlinelibrary.wiley.com/terms-and-conditions) on Wiley Online Library for rules of use; OA articles are governed by the applicable Conditions (https://onlinelibrary.wiley.com/terms-and-conditions) on Wiley Online Library for rules of use; OA articles are governed by the applicable Conditions (https://onlinelibrary.wiley.com/terms-and-conditions) on Wiley Online Library for rules of use; OA articles are governed by the applicable Conditions (https://onlinelibrary.wiley.com/terms-and-conditions) on Wiley Online Library for rules of use; OA articles are governed by the applicable Conditions (https://onlinelibrary.wiley.com/terms-and-conditions) on Wiley Online Library for rules of use; OA articles are governed by

Table 1
Model Parameters That Are Held Fixed in All Simulations

Parameter	Symbol	Value	Units	References
	Symbol			References
Gravitational acceleration	g	9.81	m s ⁻²	
Radius of large particle	r_L	250	μm	Alldredge and Silver (1988)
Porosity of small particle	$\phi_{\scriptscriptstyle S}$	0		
Proportionality constant for export partitioning ^a	κ_L	1		
Density of POM	$\rho_{\rm POM}$	1.06	$\rm g~cm^{-3}$	
Density of CaCO ₃	$ ho_{\mathrm{CaCO_3}}$	2.71	$\rm g~cm^{-3}$	
Density of opal	$ ho_{ m SiO_2}$	2.10	$\rm g~cm^{-3}$	
Molecular weight of carbon	MW_C	12	g/mol	
Molecular weight of CaCO ₃	MW_{CaCO_3}	100	g/mol	
Molecular weight of opal	$MW_{SiO_2} \\$	60	g/mol	
Mass ratio of organic matter to carbon	α	2.7		Sarmiento and Gruber (2006)
Calcite dissolution rate constant ^b	k_{calc}	For $0.8 < \Omega_{\rm calc} < 1, 4.33 \times 10^{-6}$; for $\Omega_{\rm calc} \leq 0.8, 0.0137$	$mol \ m^{-2} \ d^{-1}$	Naviaux et al. (2019)
Calcite dissolution reaction order	$n_{ m calc}$	For $0.8 < \Omega_{\rm calc} < 1, 0.11$; for $\Omega_{\rm calc} \le 0.8, 4.7$		Naviaux et al. (2019)
Aragonite dissolution rate constant ^c	$k_{ m arag}$	For $\Omega_{\rm arag} < 1$, 5.28×10^{-5}	$mol \ m^{-2} \ d^{-1}$	Dong et al. (2019)
Aragonite dissolution reaction order	$n_{ m arag}$	For $\Omega_{\text{arag}} < 1$, 1.37		Dong et al. (2019)
Specific surface area of small particle calcite	$SSA_{calc_{\mathcal{S}}}$	1040	$m^2 mol^{-1}$	Subhas et al. (2018)
Specific surface area of large particle calcite	SSA_{calc_L}	430	$m^2 mol^{-1}$	Subhas et al. (2018)
Specific surface area of aragonite	$\mathrm{SSA}_{\mathrm{arag}}$	217	$m^2 mol^{-1}$	Honjo and Erez (1978)

^aConstant of proportionality between the fraction of POC/calcite export entering the large particle size class, σ_L , and the relative abundance of opal and aragonite export (see Equation 3). ^bFor $\Omega_{\rm calc} \geq 1$, $k_{\rm calc} = 0$. ^cFor $\Omega_{\rm arag} \geq 1$, $k_{\rm arag} = 0$.

For an arbitrary size class, the bulk density of the particle, ρ_{ptcl}^{X} , is equal to the density of the solids (POM, CaCO₃, and opal) plus any porewater (seawater):

$$\rho_{\text{ptcl}}^{X} = (1 - \phi_X) \, \rho_{\text{solid}}^{X} + \phi_X \rho_{\text{sw}}, \tag{5}$$

where ϕ_X is the prescribed porosity of the small or large particle (see Tables 1 and 2) and ρ_{solid}^X is the total density of the various debris making up the small or large particle (i.e., solid particle density).

For an arbitrary size class, the solid particle density, ρ_{solid}^X , is given by the total mass of particulate matter per unit volume of seawater divided by the total volume of particulate matter per unit volume of seawater:

$$\rho_{\text{solid}}^{X} = \frac{\left[\text{POM}^{X}\right]^{+} + \left[\text{CaCO}_{3}^{X}\right]^{+} + \left[\text{SiO}_{2}^{X}\right]^{+}}{\left[\text{POM}^{X}\right]^{+}/\rho_{\text{POM}} + \left[\text{CaCO}_{3}^{X}\right]^{+}/\rho_{\text{CaCO}_{3}} + \left[\text{SiO}_{2}^{X}\right]^{+}/\rho_{\text{SiO}_{2}}},\tag{6}$$

where $[POM^X]^+$, $[CaCO_3^X]^+$, and $[SiO_2^X]^+$ are the mass concentrations (in g m⁻³) of POM, CaCO₃ (calcite + aragonite), and opal in the small or large particle size class, and ρ_{POM} , ρ_{CaCO_3} , and ρ_{SiO_2} are the prescribed densities of POM, CaCO₃, and opal in units of g m⁻³ (see Table 1). The masses of POM, CaCO₃, and opal per unit volume of seawater are derived from the tracer concentrations POC^X, $^{calc}CaCO_3^X$, $^{arag}CaCO_3^X$, and SiO_2^X :

$$\left[POM^{X} \right]^{+} = \left[POC^{X} \right] MW_{C}\alpha, \tag{7}$$

$$\left[\operatorname{CaCO}_{3}^{X}\right]^{+} = \left(\left[\operatorname{calc}\operatorname{CaCO}_{3}^{X}\right] + \left[\operatorname{arag}\operatorname{CaCO}_{3}^{X}\right]\right)\operatorname{MW}_{\operatorname{CaCO}_{3}},\tag{8}$$

$$\left[\operatorname{SiO}_{2}^{X}\right]^{+} = \left[\operatorname{SiO}_{2}^{X}\right] \operatorname{MW}_{\operatorname{SiO}_{2}}, \tag{9}$$

DINAUER ET AL. 5 of 34

Table 2Model Parameters That Are Varied in the Full Factorial Experiment: (a) Small Particle Radius, r_s ; (b) Large Particle Porosity, ϕ_L ; (c) POC Remineralization Rate Constant, k_{POC} Referenced to a Specific Temperature, in Parentheses; (d) Remineralization Rate Increase per 10°C Increase, Q_{10} ; and (e) Half-Saturation Constant for Oxygen Uptake, K_O ,

Parameter	Observed values	Mean value	Description	References
<i>r_s</i> (μm)	5, 7.5, 10	15.625	Nanoplankton ^a	Durkin et al. (2015), Richardson (2019)
	12.5, 15, 20, 25, 30		Small particles ^b	
$\phi_L(\%)$	95, 96, 97, 98, 99	97	Aggregates	Alldredge and Gotschalk (1988), Ploug, Iversen, and Fischer (2008)
$k_{\rm POC}$ (d ⁻¹)	0.02 (8°C), 0.038 (21°C), 0.066 (21°C), 0.078 (20°C), 0.144 (20°C), 0.2 (18°C)	0.122 (16.47°C)	POM ^c	Grill and Richards (1964); Garber (1984), Westrich and Berner (1984), Seiki et al. (1991)
	0.03 (4°C), 0.08 (15°C), 0.089 (16°C), 0.11 (17°C), 0.12 (15°C), 0.13 (15°C), 0.13 (20°C), 0.15 (15°C), 0.21 (15°C)		Aggregates and fecal pellets	Ploug et al. (1999), Ploug and Grossart (2000), Grossart and Ploug (2001), Ploug, Iversen, Koski, and Buitenhuis (2008), Iversen et al. (2010), Iversen and Ploug (2010), Iversen and Ploug (2013)
	0.16 (20°C), 0.32 (20°C)		Optimized with data- constrained model	DeVries and Weber (2017)
Q_{10} (unitless)	1.8, 1.88, 1.94, 3.3, 3.63, 3.9	2.29	Measured, or experimentally determined	Eppley (1972), White et al. (1991), Seiki et al. (1991); Thamdrup and Fleischer (1998), Iversen and Ploug (2013), Brewer and Peltzer (2016)
	1.51, 1.74, 2.01, 2.1, 2.4, 2.5		Determined empirically with data-constrained model	DeVries and Weber (2017), Laufkotter et al. (2017), Weber and Bianchi (2020)
K_{O_2} (µmol L ⁻¹)	1, 2, 3, 4	8.25	Experimentally determined	Devol (1978)
	8, 12, 16, 20		Determined empirically with data-constrained model	DeVries and Weber (2017), Laufkötter et al. (2017)

Note. Parameters are allowed to take on "realistic" values, which are defined as observed values in the literature. The means of the literature-based parameter values (third column) are used to define the "base-case" point in the parameter space for the purpose of the sensitivity analysis.

where MW_C , MW_{CaCO_3} , and MW_{SiO_2} are the molecular weights of carbon, $CaCO_3$, and opal in units of g/mol and α is the mass ratio of organic matter to carbon, i.e., the POM:POC mass ratio (see Table 1). For simplicity, we neglect the effect of increasing pressure with depth on bulk particle densities.

2.1.1.3. Microbial Remineralization of POC

The respiratory decomposition of organic matter is parameterized in the model using first-order kinetics. The POC remineralization rate constant, k'_{POC} , depends on ocean temperature T and dissolved oxygen O_2 :

$$k'_{POC} = k_{POC} e^{b_T (T - T_{ref})} \frac{O_2}{K_{O_2} + O_2},$$
 (10)

where $k_{\rm POC}$ is the base remineralization rate constant (in time⁻¹) referenced to temperature $T_{\rm ref}$ (in °C), $e^{b_T(T-T_{\rm ref})}$ is the modification of $k_{\rm POC}$ by temperature, and $\frac{{\rm O_2}}{K_{{\rm O_2}}+{\rm O_2}}$ is the oxygen limitation of $k_{\rm POC}$. The exponent b_T (in °C⁻¹) in the temperature modification function is trivially related to the remineralization rate increase per 10°C increase, i.e., Q_{10} , by

$$Q_{10} = e^{10b_T}. (11)$$

Because they are easier to conceptualize, Q_{10} values will be used in this paper instead of b_T values. Oxygen limitation is parameterized using Michaelis-Menten kinetics, where K_{O_2} is the half-saturation constant for oxygen uptake. The parameter values chosen for k_{POC} , Q_{10} , and K_{O_2} are shown in Table 2.

DINAUER ET AL. 6 of 34

^aOperationally defined by 20 μm diameter filter. ^bOperationally defined by 51 μm diameter filter. ^cReactive marine algal POM, or labile marine planktonic POM.

2.1.1.4. Dissolution of CaCO₃ Minerals

The rate of $CaCO_3$ dissolution, R_{CaCO_3} , is given by the empirically derived expression:

$$R_{\text{CaCO}_3} = k(1 - \Omega)^n$$
, for $\Omega < 1$, (12)

where k is the dissolution rate constant in units of time⁻¹, Ω is the saturation state of seawater with respect to the CaCO₃ mineral of interest, and n is the reaction order. In this expression, $(1 - \Omega)$ is the fractional extent of undersaturation where Ω represents the thermodynamic driving force for dissolution of calcite (Ω_{calc}) or aragonite (Ω_{arag}). k and n are empirically determined variables. k and n values from Naviaux et al. (2019) and Dong et al. (2019) are used for calcite and aragonite dissolution, respectively (see Table 1). Their rate constants (in mol m⁻² time⁻¹) are converted to units of time⁻¹ by multiplying by the specific surface area SSA of CaCO₃ particles. The SSA of small and large calcite component particles is set to that of coccoliths, $SSA_{calc_S} = 1,040 \text{ m}^2 \text{ mol}^{-1}$, and planktonic foraminifera, $SSA_{calc_L} = 430 \text{ m}^2 \text{ mol}^{-1}$, respectively (Subhas et al., 2018), whereas the SSA of aragonite is set to that of aragonitic pteropods, $SSA_{arag} = 217 \text{ m}^2 \text{ mol}^{-1}$ (Honjo & Erez, 1978).

2.1.1.5. Dissolution of Opal

The temperature sensitivity of opal solubility suggests that the rate at which opal dissolves is faster in warm waters than in cold waters. The model incorporates the effect of temperature on opal dissolution using the Arrhenius-type equation from Gnanadesikan (1999):

$$k_{\text{opal}} = 1.32 \times 10^{16} e^{\frac{-11481}{T_K}},$$
 (13)

where $k_{\rm opal}$ is the first-order opal dissolution rate constant in units of d⁻¹ and T_K is the absolute temperature (in Kelvin) of seawater. This equation results in $k_{\rm opal}$ values of 0.25 d⁻¹ (equivalent to 1/(4 d)) at 25°C and 0.01 d⁻¹ (equivalent to 1/(100 d)) at 2°C.

2.1.1.6. Large Particle Fragmentation

The fragmentation of large particles is parameterized in the model as a first-order reaction with rate constant k_{frag}^L . For simplicity, we assume k_{frag}^L (in d⁻¹) decreases exponentially with depth following Briggs et al. (2020):

$$k_{\text{frag}}^L = 0.27e^{-0.0024z},$$
 (14)

where z is depth (in m). This empirically derived function was obtained by simultaneously tracking changes in the concentrations of large and small particles over depth and time. It is assumed that $k_{\rm frag}^L$ encompasses all physical (e.g., turbulence-generated shear stress) and biological (e.g., zooplankton "sloppy feeding" and swimming behavior) processes that fragment large particles into smaller ones.

2.1.2. Model Parameter Values

The various choices of parameter values are summarized in Tables 1 and 2. In this study, r_s , ϕ_L , k_{POC} , Q_{10} , and K_{O_2} are treated as adjustable parameters (see Section 2.2.1). All other parameters are held constant in the model simulations. r_L is assumed to correspond to the minimum radius of macroscopic aggregates, operationally defined as 250 µm (Alldredge & Silver, 1988), whereas ϕ_s is assumed to be zero. Laboratory studies show that porosity decreases significantly with decreasing particle size (e.g., Alldredge & Gotschalk, 1988; Logan & Wilkinson, 1990). The treatment of r_L and ϕ_s as fixed parameters is motivated primarily by the need to reduce the number of model runs required for the full factorial design. These two parameters could be revisited in future work, although new observational constraints are needed to limit the model's dynamical freedom.

2.1.3. Grid Resolution and Model Configuration

The model equations are implemented on a 1° latitude–longitude grid with 26 levels in the vertical. The horizontal grid is the standard 1° grid used by the World Ocean Atlas (WOA) (Levitus, 1982; Locarnini et al., 2013). The vertical grid is based on the WOA's 33 standard depth levels. Here, the depth coordinates on the vertical tracer grid are from 112.5 to 5,250 m with grid cells ranging in thickness from 25 to 500 m. The ocean state variables (temperature, dissolved oxygen, density, viscosity, and calcite and aragonite saturation states) are prescribed using observation-based climatologies (see Appendix A1 for more details). The advective flux

DINAUER ET AL. 7 of 34

divergence term, $-\frac{\partial \left(w_{\text{sink}}^X \left[C^X\right]\right)}{\partial z}$, is determined from a first-order "upwind" tracer advection scheme. The model is run with a prescribed surface forcing until it reaches equilibrium. The surface boundary fluxes used to force the model are POC, calcite, aragonite, and opal export fluxes taken from the Coupled Model Intercomparison Project Phases 5 and 6 (CMIP5 and CMIP6). A multi-model ensemble median is constructed for each of the forcing fields from two CMIP5 and five CMIP6 models (see Appendix A2 for further details). The time step used in this study is 5,400 s (1.5 hr), which was chosen so as not to deplete the smallest vertical grid cell over the time step given the estimated maximum probable particle settling velocity. The model is integrated for at least two sinking small particle residence times ($\geq 1,080$ days), during which the model reaches equilibrium. The wall-clock time required to run the model, per horizontal grid point and on a single CPU core, is roughly 12 s.

This study makes use of two different configurations of the MSPACMAM. The default model configuration, also referred to as the std configuration, does not include large particle fragmentation, whereas the impacts of fragmentation are explicitly resolved in a second model configuration (so-called frag configuration). Note that, although model runs are performed using both the std and frag configurations, discussion of the model results will focus mainly on the std configuration, given that the generality of the empirical specific fragmentation rate function of Briggs et al. (2020) is uncertain. Note also that the MSPACMAM can be configured to represent a physically protected fraction of POC that is inaccessible to remineralization due to the association with calcite minerals. However, the present study does not make use of this configuration as there is insufficient evidence to suggest that ballast minerals provide physical protection for labile POC against bacterial activity (Iversen & Ploug, 2010; Ploug, Iversen, & Fischer, 2008, Ploug, Iversen, Koski, & Buitenhuis, 2008).

2.2. Sensitivity Analysis and Model Evaluation

We explore the sensitivity of model output to five input parameters $(r_5, \phi_L, k_{POC}, Q_{10}, and Ko_2)$ thought to be important for POC flux attenuation with depth. A sensitivity analysis is conducted for three main reasons: (a) to assess how the POC flux profile shape responds to changes in each parameter, (b) to determine which parameters contribute most to the variability (or uncertainty) in $T_{\rm eff}$, and (c) to find combinations of parameter values yielding model results that agree well with available observations. The identification of the most sensitive parameters in the model serves (a) to provide direction for future research so that the uncertainties of the influential parameters are reduced and (b) to guide future calibration efforts such that computational resources are allocated to constraining important parameters.

2.2.1. Full Factorial Experiment

Model simulations are performed with different choices of parameter values. Each parameter is allowed to take on observed values selected from the literature (see Table 2). A full factorial design is used to explore the 5D parameter space, which required $9 \times 5 \times 18 \times 13 \times 9 = 94,770$ runs of the model for each of the configurations (std and frag). The model is run only at the 26 horizontal grid points where evaluation data are available (see Section 2.2.3.1 and Figure 1).

2.2.2. Differential Sensitivity Analysis

A widely used approach to sensitivity analysis is differential analysis, which is based on the calculation of first-order partial derivatives of the output variable of interest with respect to the input parameters at a "base-case" point in the parameter space (Hamby, 1994; Iman & Helton, 1988; Pianosi et al., 2016). The partial derivatives are used as sensitivity indices (or importance measures) to discriminate between influential and noninfluential parameters. The purpose of the differential analysis applied here is to identify the input parameters that exert the most influence on the model's mean $T_{\rm eff}$ response, $\overline{T_{\rm eff}}$. Depending on the analysis, $T_{\rm eff}$ is averaged either over the 26 data locations or over a subset of data locations belonging to a distinct ocean regime. $\overline{T_{\rm eff}}$ is recorded for each model run (parameter set) in the factorial design prior to performing the differential analysis.

The base-case point is defined as the mean values of the input parameters $p_1, ..., p_n$, \overline{p} . The partial derivative $\frac{\partial \overline{T_{\rm eff}}}{\partial p_i}$ evaluated at \overline{p} can be thought of as the local sensitivity of $\overline{T_{\rm eff}}$ to input parameter p_i . Here, the partial derivatives are numerically approximated as finite differences. To remove the effect of units, each partial derivative is normalized as $\left(\partial \overline{T_{\rm eff}}/\partial p_i\right)\left(p_{i0}/\overline{T_{\rm eff_0}}\right)$ where p_{i0} is the base-case (mean) value of p_i and $\overline{T_{\rm eff_0}}$ is the $\overline{T_{\rm eff}}$ predicted

DINAUER ET AL. 8 of 34

19449224, 2022, 10, Downloaded from https://agupubs.onlinelibrary.wiley.com/doi/10.1029/2021GB007131, Wiley Online Library on [18/11/2024]. See the Terms and Conditions (https://onlinelibrary.wiley.com/term

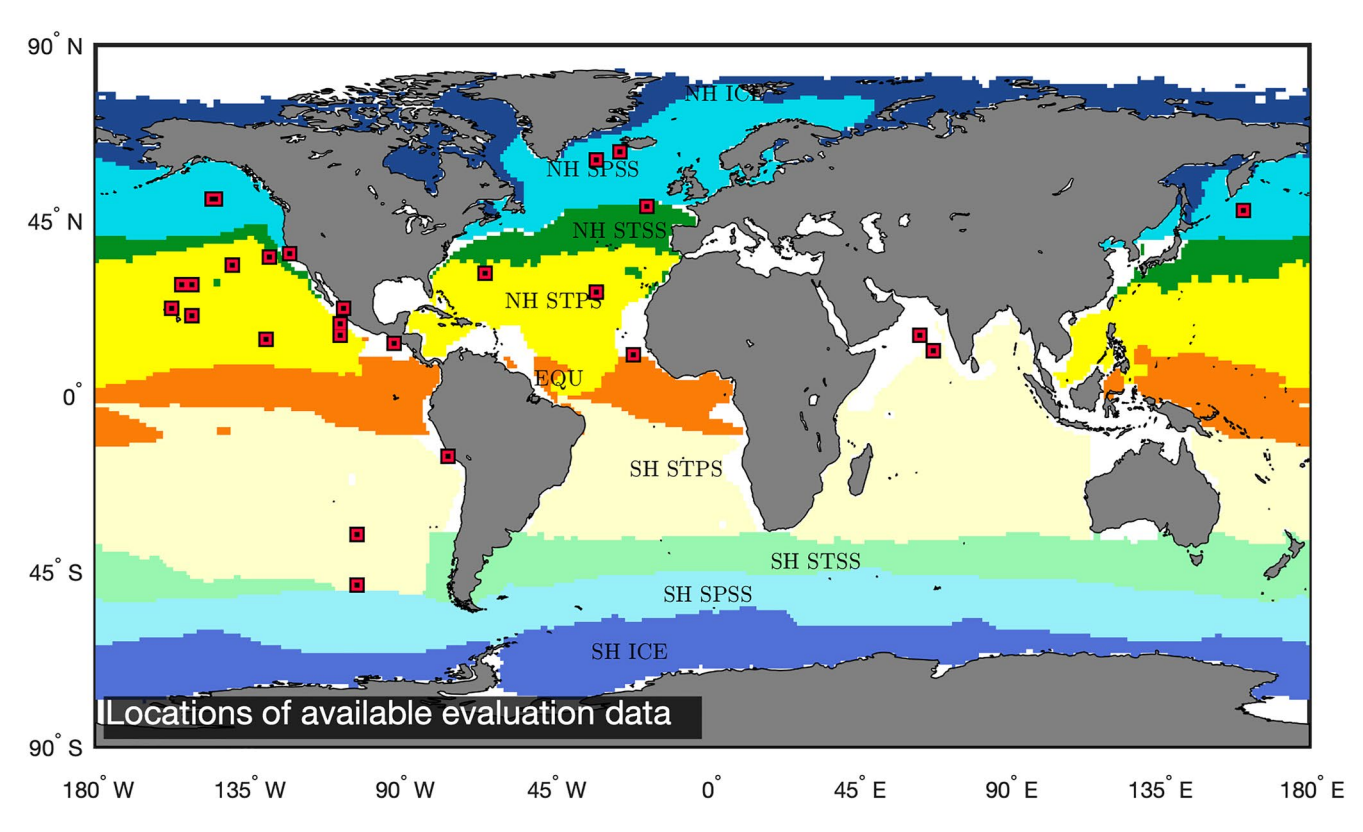


Figure 1. Global map of the locations of the observations used for model evaluation. Available evaluation data include trap-derived sinking POC flux measurements and tracer-based oxygen consumption rate data. Also shown is the global distribution of open-ocean biomes adapted from Fay and McKinley (2014). NH ICE is the northern hemisphere marginal sea ice zone; NH SPSS is the northern hemisphere subpolar gyre; NH STSS is the northern hemisphere intergyre region; NH STPS is the northern hemisphere subtropical gyre; SH STSS is the Southern Ocean seasonally stratified subtropics (or Subantarctic Zone, SAZ); SH SPSS is the Southern Ocean subpolar gyre (or Polar Frontal Zone, PFZ); and SH ICE is the Southern Ocean marginal sea ice zone (or Antarctic Zone, AZ).

by base-case values \overline{p} . These standardized partial derivatives, also referred to as normalized sensitivity coefficients S_i , are used for parameter ranking.

The variance of $\overline{T_{\rm eff}}$ due to parameter uncertainties, $Var\left(\overline{T_{\rm eff}}\right)$, is estimated using the general error propagation formula. $Var\left(\overline{T_{\rm eff}}\right)$ is treated as a function of the input parameters and approximated with a first-order Taylor series expansion at \overline{p} :

$$\operatorname{Var}\left(\overline{T_{\mathrm{eff}}}\right) = \sum_{i=1}^{n} \left(\frac{\partial \overline{T_{\mathrm{eff}}}}{\partial p_{i}}\right)^{2} \operatorname{Var}\left(p_{i}\right),\tag{15}$$

where $\operatorname{Var}(p_i)$ is the variance of the literature-based values of p_i . Here, the input parameters are assumed to be independent of one another. While it is only an approximation, the advantage of using the Taylor series expansion in Equation 15 is that it quantifies the relative importance of each parameter's sensitivity versus variability as well as its percentage contribution to the estimated variance of $\overline{T_{\rm eff}}$, i.e., $\left(\frac{\partial \overline{T_{\rm eff}}}{\partial p_i}\right)^2 \operatorname{Var}(p_i) / \operatorname{Var}\left(\overline{T_{\rm eff}}\right) \times 100$.

2.2.3. Evaluation of Model Performance

The 94,770 model runs, each with a different parameter set, are evaluated against available observations using a cost function that summarizes the model-data misfit. The combinations of parameter values yielding the lowest cost are referred to as the best performing parameter sets.

DINAUER ET AL. 9 of 34

onlinelibrary.wiley.com/doi/10.1029/2021GB007131, Wiley Online Library on [18/11/2024]. See the Term

2.2.3.1. Observational Constraints

Observations of the sinking POC flux and oxygen consumption rate are used to evaluate model performance at 26 locations across the global ocean (see Figure 1). We have compiled a collection of 22 POC flux profiles (defined here as >2 flux observations in the mesopelagic zone) measured either with free-drifting sediment traps (i.e., surface tethered and neutrally buoyant sediment traps) or with Marine Snow Catchers. The compilation includes data from Martin et al. (1987), Devol and Hartnett (2001), Van Mooy et al. (2002), Buesseler et al. (2007), Owens et al. (2013), Durkin et al. (2015), Marsay et al. (2015), Keil et al. (2016), Engel et al. (2017), and Cavan et al. (2017). We have also incorporated results from the recent EXPORTS program, which are available online at https://seabass.gsfc.nasa.gov/. Five observation-based oxygen consumption rate profiles (Sonnerup et al., 2013, 2015; Stanley et al., 2012) are selected from the compilation of Brewer and Peltzer (2017). In order to make use of these observations, model-predicted POC remineralization rates are combined with DOC remineralization rates from the data-assimilated biological pump model of DeVries and Weber (2017) and multiplied by a O₂:C stoichiometric ratio of 170:117 (Anderson & Sarmiento, 1994).

2.2.3.2. Model Performance Metrics

A cost function J is used to evaluate model performance with each of the 94,770 parameter sets. J is expressed as a weighted sum of squared differences between model predictions (P) and observations (O):

$$J = \sum_{v=1}^{M} \frac{1}{N_v} \left(\frac{C_v}{\sigma_v}\right)^2 \sum_{i=1}^{N_v} (P_{vi} - O_{vi})^2, \tag{16}$$

where M=2 is the number of different data types or variables (i.e., sinking POC flux $F_{\rm POC}$ and oxygen consumption rate OUR), N_v is the number of model grid cells where observations are available for variable v, and P_{vi} and O_{vi} are the predicted and observed values of variable v at grid cell i. To account for differing units, the weight given to each variable is inversely proportional to the square of the standard deviation of its observations, σ_v (Friedrichs et al., 2007; Kuhn et al., 2018; Kuhn & Fennel, 2019; Xiao & Friedrichs, 2014). The weighting factor, C_v , is included to increase the weight of $F_{\rm POC}$ since it is the output variable of most interest. Here, $C_{F_{\rm POC}}$ is set to 3 and $C_{\rm OUR}$ to 1. The POC flux profiles were normalized to the flux at the shallowest depth at which observations are available, the oxygen consumption rate data were log transformed, and all observations were binned to the model grid prior to calculating J.

Best performing parameter sets are defined as all parameter sets yielding cost values within 1% of the minimum cost value. This threshold value of 1% is used to reduce the number of "acceptable solutions" to a manageable size. In addition to cost values, model performance is quantified with four univariate statistical measures (Stow et al., 2009): (a) the standard deviation of the predictions relative to the observed standard deviation, i.e., $\sigma_{mod}/\sigma_{obs}$, (b) the correlation coefficient, r, (c) the root-mean-square error (RMSE), and (d) the normalized RMSE, NRMSE = RMSE/ σ_{obs} .

2.3. Analysis of Global Transfer Efficiency Variability

2.3.1. Model Experiments

Global model simulations are performed to provide insight into six environmental factors $\mathrm{EF}_1,\ldots,\mathrm{EF}_n$ thought to be important for controlling the spatial pattern of T_{eff} , i.e., ocean temperature, dissolved oxygen, seawater density, seawater viscosity, particle size, and particle density. These factors will be denoted by T, O_2 , ρ_{sw} , visc, σ_L , and ρ_{PM} , respectively. Table 3 summarizes the suite of model experiments utilized for the analysis of global T_{eff} variability. The baseline simulation (ctrl) provides a benchmark for the spatial pattern of T_{eff} . Idealized experiments have been designed to remove spatial variations in $\mathrm{EF}_1,\ldots,\mathrm{EF}_n$ one at a time. In the case of T, O_2 , ρ_{sw} , and visc, the model is run with 3D fields set to global mean mesopelagic values. Note that the temperature adjustment applies only to the temperature field used to calculate the rate of POC remineralization (see Equation 10). Particle size variability is removed by setting the σ_L distribution to the global mean of 0.154 from the ctrl simulation. To remove particle density variations, the bulk particle densities of the small and large size classes, ρ_{ptcl}^S and ρ_{ptcl}^L , are prescribed rather than calculated interactively (Equation 5). ρ_{ptcl}^S is set to the global mesopelagic mean of 1.536 g cm⁻³ from the ctrl simulation, and ρ_{ptcl}^L is likewise set to 1.052 g cm⁻³.

DINAUER ET AL. 10 of 34

Table 3 Overview of Model Experiments Utilized for the Analysis of Global T_{eff} Variability

Experiment name	Abbreviation	Description
Baseline or control	ctrl	Model allows all environmental factors to vary in space
Constant temperature	\overline{T}	Model assumes ocean temperature ^a is spatially uniform at the global mesopelagic mean of 7.26°C
Constant oxygen	$\overline{O_2}$	Model assumes dissolved oxygen is spatially uniform at the global mesopelagic mean of 195 mmol $\rm m^{-3}$
Constant seawater density	$\overline{ ho_{sw}}$	Model assumes seawater density is spatially uniform at the global mesopelagic mean of $1029\ kg\ m^{-3}$
Constant viscosity	visc	Model assumes seawater viscosity is spatially uniform at the global mesopelagic mean of $0.0015\ kg\ m^{-1}\ s^{-1}$
Constant particle size	$\overline{\sigma_L}$	Model assumes POC export allocation fraction σ_L is spatially uniform at the global mean of 0.154
Constant particle density	$\overline{ ho_{ ext{PM}}}$	Model assumes small and large particle densities $\rho_{\rm ptcl}^S$ and $\rho_{\rm ptcl}^L$ are spatially uniform at their global mean mesopelagic values of 1,536 kg m ⁻³ and 1,052 kg m ⁻³ , respectively

Note. The baseline model simulation (or control simulation) provides a benchmark for the spatial pattern of $T_{\rm eff}$. The idealized experiments target six key environmental factors controlling the large-scale $T_{\rm eff}$ pattern: ocean temperature, dissolved oxygen, seawater density, seawater viscosity, particle size, and particle density (see Section 2.3.1 for more details).

^aThe temperature field used to calculate the rate of POC remineralization (see Equation 10).

2.3.2. Deconvolving the Environmental Factors

The contribution of environmental factor EF_i to the spatial pattern of T_{eff} is estimated by the difference between the patterns of T_{eff} for ctrl and an experiment in which EF_i is forced to be spatially uniform:

$$\Delta T_{\text{eff}}^{EF_i}(\text{lat}, \text{lon}) = T_{\text{eff}}^{\text{ctrl}}(\text{lat}, \text{lon}) - T_{\text{eff}}^{\overline{EF_i}}(\text{lat}, \text{lon}), \tag{17}$$

where $\Delta T_{\rm eff}^{EF_i}$ is the component of the $T_{\rm eff}$ pattern attributable to ${\rm EF}_i$ variability, $T_{\rm eff}^{ctrl}$ is the $T_{\rm eff}$ pattern from ctrl, and $T_{\rm eff}^{EF_i}$ is the $T_{\rm eff}$ pattern from an experiment in which the spatial variations in ${\rm EF}_i$ have been removed (Table 3). It should be noted that there is less confidence in $\Delta T_{\rm eff}^{\sigma_L}$ and $\Delta T_{\rm eff}^{\rho_P M}$ than in the other environmental components, since the particle size and density information used to drive the model equations is diagnosed by the model itself, rather than derived from observation-based climatologies as is the case for seawater temperature, density, viscosity, and dissolved oxygen. Nonetheless, the broad spatial features should be properly manifested in the $\Delta T_{\rm eff}^{\sigma_L}$ and $\Delta T_{\rm eff}^{\rho_P M}$ patterns.

3. Results and Discussion

3.1. Model-Data Comparisons

The performance of the MSPACMAM is evaluated against observed sinking POC fluxes and oxygen consumption rates at 26 locations across the global ocean (see Figure 1). Cost function values are similar across a large portion of the parameter sets (Figure 2), indicating that different combinations of parameter values yield equally plausible model solutions. The shape of the vertical POC flux profile results from the balance between the rates of particle sinking and POC remineralization. Without sufficient observations to constrain one or both of these terms, there are many different ways of reproducing the same balance. As a consequence, there is not a single, unique set of parameter values that outperforms the others.

The ranges of the best performing parameter sets, defined here as parameter sets within 1% of the minimum cost value, are shown in Table 4. The best-fit parameter values span much of the literature-based ranges, with the exception of Q_{10} and K_{O_2} whose low-cost values lie at the lower end of their possible ranges. The parameter combinations within 5% of the minimum cost value span even wider ranges as shown in Table B1. The subset of best-fit parameter combinations with a slower rate of POC remineralization (i.e., $k_{\rm POC}$ below the 50th percentile) exhibit a slower rate of particle sinking, which can be explained by smaller particles in the small size class

DINAUER ET AL. 11 of 34

9449224, 2022, 10, Downloaded from https://agupubs.onlinelibrary.wiley.com/doi/10.1029/2021GB007131, Wiley Online Library on [18/11/2024]. See the Terms and Conditions

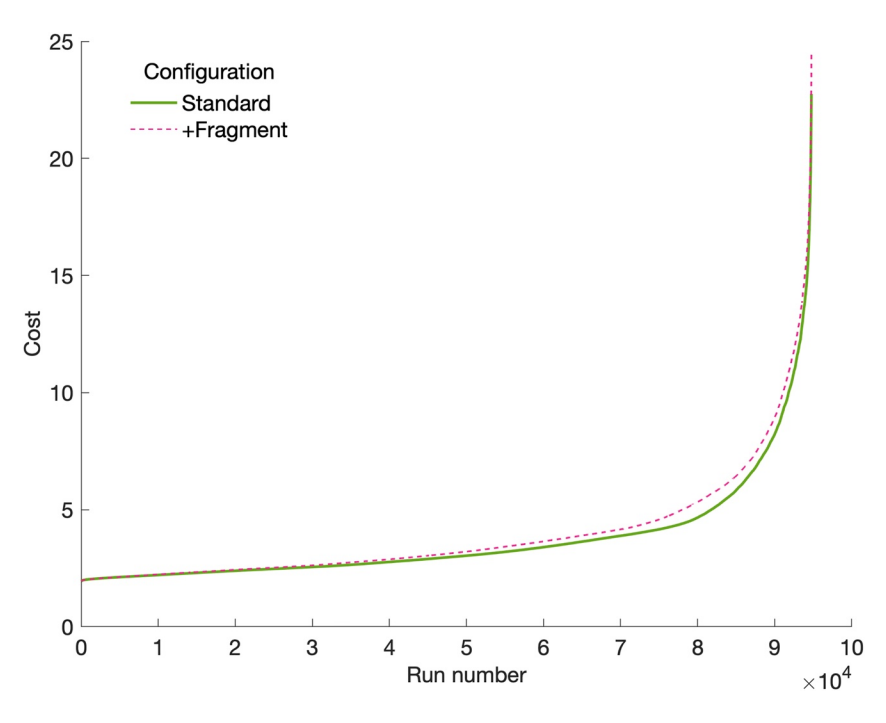


Figure 2. Value of the cost function, J, as a function of model parameter set for two different configurations. The run number is an arbitrary label corresponding to a discrete parameter set from the full factorial experiment, in which 94,770 literature-based parameter combinations were tested.

 $(\overline{r_S} = 13.8 \ \mu\text{m})$ and more porous large particles $(\overline{\phi_L} = 96.9\%)$. In contrast, when the rate of remineralization is faster (i.e., k_{POC} above the 50th percentile), the rate of sinking is also faster $(\overline{r_S} = 20.3 \ \mu\text{m})$ and $\overline{\phi_L} = 95.7\%$. This demonstrates that the observed POC flux attenuation with depth can be achieved either by slow sinking combined

Table 4 *Means and Ranges of the Best Performing Parameter Sets in the 94,770-Run Factorial Experiment*

	r_S (µm)	$\phi_L(\%)$	k_{POC}^{ref} (d ⁻¹) ^a	Q_{10} (unitless)	$K_{\mathrm{O}_2}(\mu\mathrm{mol}\ \mathrm{L}^{-1})$
A priori	5-30	95–99	0.033-0.32	1.51-3.9	1–20
		Stand	lard configurat	ion (N = 73)	
Mean	17.0	96.2	0.11	1.51	2.01
Range	10-25	95–99	0.037-0.22	1.51-1.51	1–3
Configuration with fragmentation ($N = 57$)					
Mean	16.4	95.4	0.10	1.51	1.79
Range	10–25	95–97	0.033-0.22	1.51-1.51	1–3

Note. The choice of threshold for defining these "acceptable solutions" is a 1% change in the minimum cost value (see Equation 16 for the cost function). For comparison, the ranges of the parameter combinations below a threshold of 5% are shown in Appendix B (Table B1).

^aThe POC remineralization rate constant, $k_{\rm POC}$, referenced to 20°C. Since the original, literature-based $k_{\rm POC}$ values are referenced to various temperatures $T_{\rm ref}$ (see Table 2), they have been normalized to a common reference temperature of 20°C by multiplying by $e^{b_T(20-T_{\rm ref})}$ where $b_T = \ln Q_{10}/10$. For $k_{\rm POC}$ in the best performing parameter sets, the accompanying Q_{10} value is used. For the a priori literature-based values of $k_{\rm POC}$, a Q_{10} value of 1.51 is used.

with slow remineralization or by fast sinking combined with fast remineralization. Observed POC flux profiles from a greater variety of biogeographical regions, along with high-quality particle sinking speed observations, are needed to better constrain the $k_{\rm POC}$, $r_{\rm S}$, and ϕ_L values.

An open question raised by sediment trap studies is whether $T_{\rm eff}$ is higher over high latitudes or higher over low latitudes. About one fourth of the literature-based parameter sets yield low-latitude $T_{\rm eff}$ that is higher than high-latitude $T_{\rm eff}$, although none are within 1% of the minimum cost value. Higher low-latitude $T_{\rm eff}$ is achieved by running the model with the combination of relatively large r_S (22.6 µm), high ϕ_L (97.4%), and high K_{O_2} (12.3 µmol L^{-1}). An important caveat is that model evaluation is limited to those locations for which observations are available, with the consequence being many of the low-latitude locations are within oxygen minimum zones (see Figure 1) where the lack of oxygen strongly inhibits microbial remineralization. We conclude that the credible representation of higher low-latitude $T_{\rm eff}$ outside oxygen minimum zones is difficult to achieve with literature-based parameter values.

Comparisons of modeled and observed normalized POC flux profiles are shown in Figure 3 for 12 of the locations where observations are available (see Figure B1 for all 22 locations). Model results are in good agreement with observations across a range of temperature and oxygen regimes (see Figure B2 and Figure B3 for the temperature and oxygen profiles at the data locations). Model performance metrics, including $\sigma_{\rm mod}/\sigma_{\rm obs}$ (a measure of the amplitude of modeled variability relative to observed variability), r (a meas-

DINAUER ET AL. 12 of 34

19449224, 2022, 10, Downloaded from https://agupubs online libary.viley.com/doi/10.1029/2021GB007131, Wiley Online Libary on [18/11/2024]. See the Terms and Conditions (https://onlinelibary.viley.com/terms-and-conditions) on Wiley Online Library for rules of use; OA articles are governed by the applicable Creative

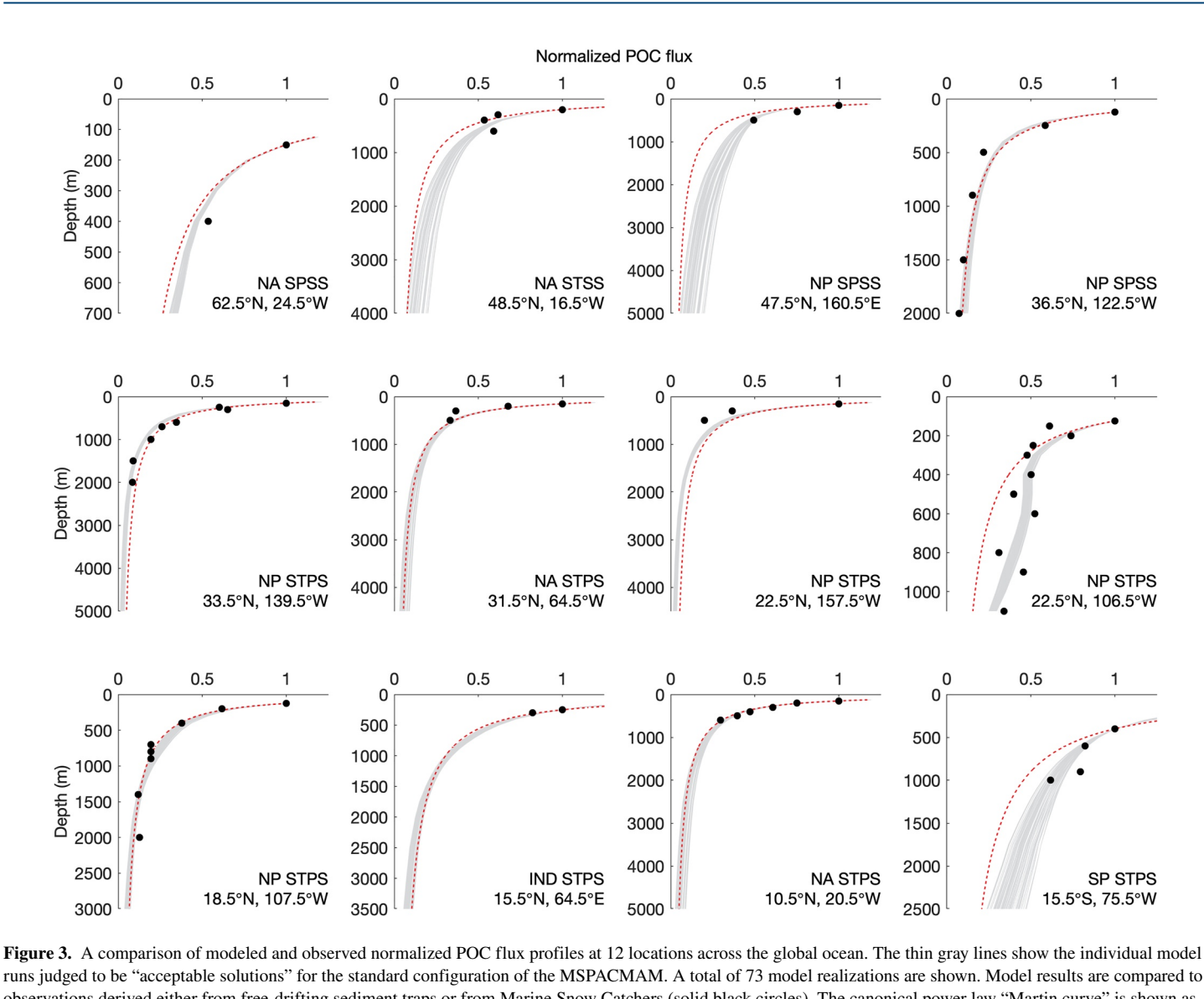


Figure 3. A comparison of modeled and observed normalized POC flux profiles at 12 locations across the global ocean. The thin gray lines show the individual model runs judged to be "acceptable solutions" for the standard configuration of the MSPACMAM. A total of 73 model realizations are shown. Model results are compared to observations derived either from free-drifting sediment traps or from Marine Snow Catchers (solid black circles). The canonical power law "Martin curve" is shown as a dashed red line for reference. The vertical POC flux profiles have been normalized by their shallowest flux in order to facilitate the comparison between predictions and observations.

ure of pattern similarity), RMSE and NRMSE (measures of the size of the model-data misfit), are provided in Table 5. The normalized error for the POC flux profiles (NRMSE = 0.35) is smaller than that for the oxygen consumption rates (NRMSE = 0.93), which is expected since the latter is a reconstruction. There is a strong positive relationship between the predicted and observed POC flux values with a correlation coefficient of 0.94. For oxygen consumption rates, the correlation between predictions and observations is weaker (r = 0.64). The ratio of the modeled to the observed standard deviation is close to 1 for both output variables. The ability of the MSPACMAM to capture important aspects of the observed variability in POC flux profiles, including amplitude and pattern, adds confidence to its generality for global-scale simulations of $T_{\rm eff}$.

3.2. Model Sensitivity to Parameter Variations

3.2.1. Response of the Vertical POC Flux Profile

Figure 4 shows the mean POC flux profiles resulting from varying each input parameter over its literature-based range, while all others are held constant at their base-case values (see Table 2). The shape of the profiles

DINAUER ET AL. 13 of 34

9449224, 2022, 10, Downloaded from https://agupubs.

and-conditions) on Wiley Online Library for rules of use; OA articles are governed by the applicable Creative Commons License

Table 5Summary of Model Performance Based on the Best Performing Parameter Sets

	Sinking POC flux (normalized)	Oxygen consumption rate (log transformed)
	Standard configuration	N = 73
$\sigma_{ m mod}/\sigma_{ m obs}$	0.96	0.89
r	0.94	0.64
RMSE	0.11 units	$3.61 \text{ mmol O}_2 \text{ m}^{-3} \text{ yr}^{-1}$
NRMSE	0.35	0.93
,	Configuration with fragmer	ntation $(N = 57)$
$\sigma_{ m mod}/\sigma_{ m obs}$	0.97	0.88
r	0.94	0.63
RMSE	0.11 units	$3.59 \text{ mmol O}_2 \text{ m}^{-3} \text{ yr}^{-1}$
NRMSE	0.35	0.92

Note. Model performance is evaluated relative to observations of the sinking POC flux and oxygen consumption rate. The model performance metrics $(\sigma_{\text{mod}}/\sigma_{\text{obs}}, r, \text{RMSE}, \text{ and NRMSE})$ are averaged over the "acceptable solutions."

reflects the strength of POC flux attenuation with depth. Larger values of r_S and lower values of ϕ_L increase bulk particle sinking speeds and therefore decrease POC flux attenuation. Higher $k_{\rm POC}$ values increase POC remineralization rates, thereby increasing flux attenuation. Increases in Q_{10} decrease remineralization rates in cold waters deeper in the water column, leading to decreased flux attenuation. Higher values of K_{O_2} result in weaker remineralization rates in oxygen deficient waters and thus lower POC flux attenuation.

The response of the POC flux profile to perturbed parameter values varies vertically. Changes in $k_{\rm POC}$ have a large impact on the sinking POC flux throughout the water column, although the deep ocean response below ~2,000 m is noticeably weaker. While the influence of $r_{\rm S}$ on the upper ocean POC flux profile is similar to that of $k_{\rm POC}$, its impact is more limited in the deep ocean (>1,000 m) where small particles become less prevalent. In contrast to $k_{\rm POC}$ and $r_{\rm S}$, the influence of ϕ_L and Q_{10} on the POC flux profile increases with increasing depth. Changes in Q_{10} induce changes in the POC remineralization rate via $k_{\rm POC} \cdot Q_{10}^{T-T_{\rm ref}/10}$. Because the base-case value of $k_{\rm POC}$ is referenced to the relatively warm temperature of 16.5°C (i.e., $T_{\rm ref}=16.5^{\circ}$ C), the deeper the depth (the colder the ocean temperatures) the stronger the influence of Q_{10} on the remineralization rate. In the case of ϕ_L , large particles contribute more to the bulk sinking POC flux with depth, and hence changes in ϕ_L have a stronger influence on the deep ocean POC fluxes. While influential at depth, ϕ_L variations have the weakest influence on the POC flux in shallow waters above ~500 m, where small particles tend to be generally

more abundant than large ones. The sensitivity of the POC flux to changes in K_{O_2} appears to be very weak except in the shallow water column from ~500 to 1,000 m, the depth range over which suboxic conditions occur at some of the 26 locations considered in this analysis (see Figure B3).

3.2.2. Sensitivity Analysis of Transfer Efficiency

3.2.2.1. Relative Influence of Model Parameters on Transfer Efficiency

To identify the most influential input parameters, we first examine the range of $\overline{T_{\rm eff}}$ output, averaged over the 26 data locations, resulting from varying each parameter over its literature-based range, while all others are held constant. Figure 5 provides a visual presentation of the magnitude of $\overline{T_{\rm eff}}$ change in response to perturbed parameter values. $k_{\rm POC}$ and $r_{\rm S}$ cause the largest variations in $\overline{T_{\rm eff}}$, with values ranging from 11.5% to 39.0% for $k_{\rm POC}$ and from 10.3% to 33.3% for $r_{\rm S}$. Variations in $\overline{T_{\rm eff}}$ are much smaller when Q_{10} , K_{O_2} , and ϕ_L are varied. $\overline{T_{\rm eff}}$ ranges between 14.1% and 21.9% for Q_{10} , 14.1% and 20.7% for K_{O_2} , and 14.0% and 18.2% for ϕ_L .

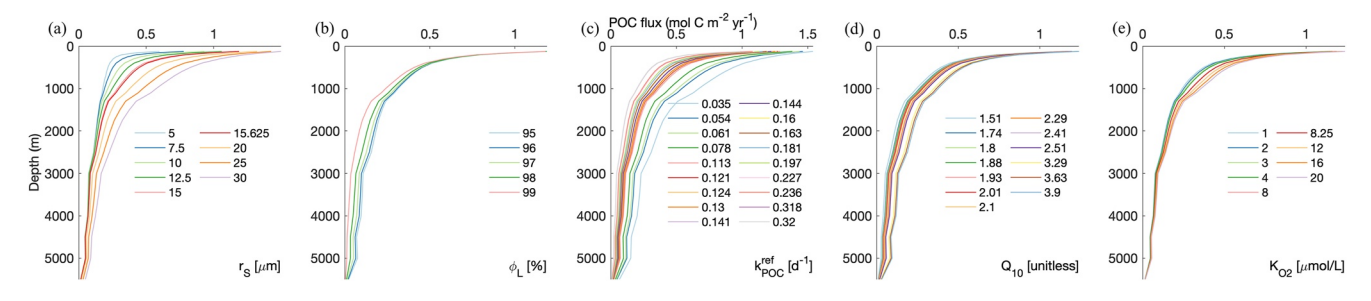


Figure 4. Mean POC flux profiles, averaged over the 26 data locations, resulting from varying input parameters one at a time over their literature-based ranges. Each parameter value is shown as a colored line. Model results are based on the standard configuration of the MSPACMAM. (a) The small particle radius, r_s , is varied from 5 to 30 μ m. (b) The large particle porosity, ϕ_L , is varied from 95% to 99%. (c) The POC remineralization rate constant referenced to 20°C, k_{POC}^{ref} , is varied from 0.035 to 0.32 d⁻¹. The original, literature-based k_{POC} values shown in Table 2 are referenced to various temperatures and therefore have been normalized to a common reference temperature of 20°C in order to place them on a comparable level for visualization purposes. (d) The remineralization rate increase per 10°C increase, Q_{10} , is varied from 1.51 to 3.9. (e) The half-saturation constant for oxygen uptake, K_{O_2} , is varied from 1 to 20 μ mol L⁻¹. Note that each parameter is varied over its literature-based range, while all others are held constant at their base-case values (i.e., their mean values).

DINAUER ET AL. 14 of 34

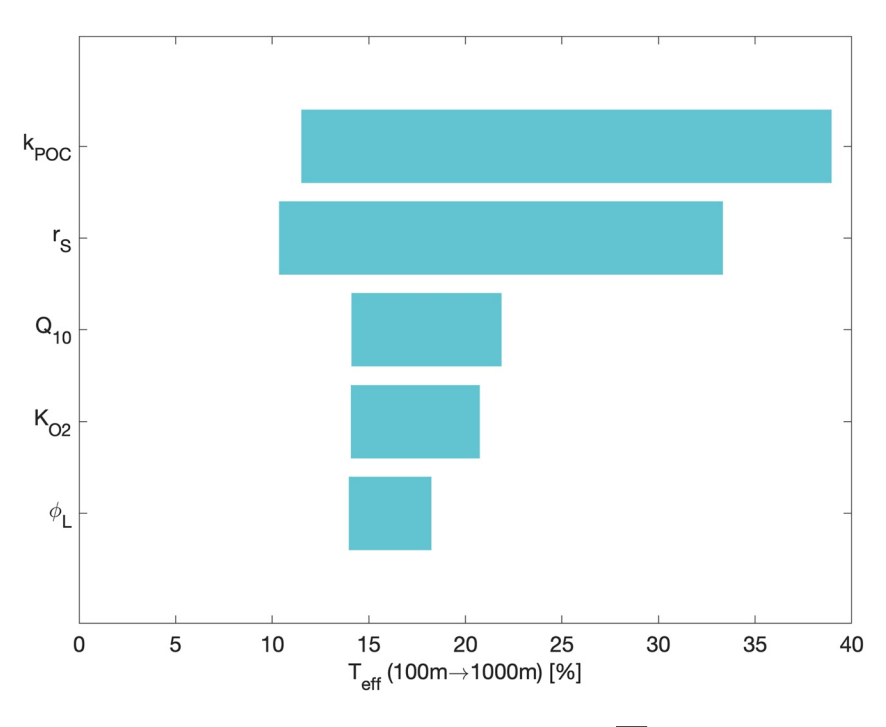


Figure 5. Graphical representation of parameter sensitivity based on the ranges of $\overline{T_{\rm eff}}$ output in response to perturbed parameter values. Horizontal bars extend the minimum and maximum $\overline{T_{\rm eff}}$ values resulting from varying each input parameter from its minimum value to its maximum value, while holding all others constant. Model output is based on the standard configuration of the MSPACMAM.

Next, we determine the rate of change of $\overline{T_{\rm eff}}$ with respect to input parameter p_i , $\frac{\delta \overline{T_{\rm eff}}}{\delta p_i}$. Based on the normalized sensitivity coefficients S_i , the most sensitive parameters in order are ϕ_L , r_S , $k_{\rm POC}$, Q_{10} , and K_{O_2} (see Table 6). The fact that $\overline{T_{\rm eff}}$ is least sensitive to Q_{10} and K_{O_2} might be expected since their impact on the $\overline{T_{\rm eff}}$ output was among the smallest. However, the high sensitivity of $\overline{T_{\rm eff}}$ to ϕ_L is a rather surprising result given that changes in ϕ_L resulted in the smallest range of $\overline{T_{\rm eff}}$ output. This underlines the importance of examining not only the range of modeled $\overline{T_{\rm eff}}$ behavior in response to p_i variations but also the rate at which $\overline{T_{\rm eff}}$ changes with respect to p_i .

 Table 6

 The Influence of Each Input Parameter, p_p on the Model's Mean T_{eff} Response Averaged Over the 26 Data Locations, $\overline{T_{eff}}$

Parameter pi	$\frac{\partial \overline{T_{\mathrm{eff}}}}{\partial p_i}$	S_{i}	$\operatorname{Var}(p_i)$	$\left(\frac{\partial \overline{T_{\rm eff}}}{\partial p_i}\right)^2 { m Var}\left(p_i\right)$	% of Var $\left(\overline{T_{\rm eff}}\right)$
r_S (µm)	0.95	0.86	66.8	60.4	52.51
$\phi_L(\%)$	-1.02	5.70	2.50	2.59	2.25
$k_{\rm POC}^{\rm ref}$ (d ⁻¹) ^a	-78.7	0.74	0.007	40.9	35.55
Q_{10} (unitless)	3.18	0.42	0.57	5.80	5.04
K_{O_2} (µmol L ⁻¹)	0.35	0.17	43.7	5.34	4.65
$\operatorname{Var}\left(\overline{T_{\mathrm{eff}}}\right)$				115.0	
SD of $\overline{T_{\rm eff}}$ (%)				10.7	

Note. The normalized sensitivity coefficients S_i shown in the third column are the partial derivatives (second column) normalized by the quotient $p_{i0}/\overline{T_{\rm eff_0}}$, where pi_0 is the base-case (mean) value of pi and $\overline{T_{\rm eff_0}}$ is the $\overline{T_{\rm eff}}$ predicted by the base-case values \overline{p} . The last column shows each parameter's percentage contribution to the estimated variance of $\overline{T_{\rm eff}}$, $Var\left(\overline{T_{\rm eff}}\right)$ (see Section 2.2.2 for more details).

^aThe POC remineralization rate constant, $k_{\rm POC}$, referenced to 20°C. Since the original, literature-based $k_{\rm POC}$ values are referenced to various temperatures $T_{\rm ref}$ (see Table 2), they have been normalized to a common reference temperature of 20°C by multiplying by $e^{b_{T0}(20-T_{\rm ref})}$, where $b_{T0}=0.0827$ is the base-case value of b_T (which is equivalent to a Q_{10} value of 2.29).

DINAUER ET AL. 15 of 34

19449224, 2022, 10, Downloaded from https://agupubs.onlinelibrary.wiley.com/doi/10.1029/2021GB007131, Wiley Online Library on [18/11/2024]. See the Terms and Conditions

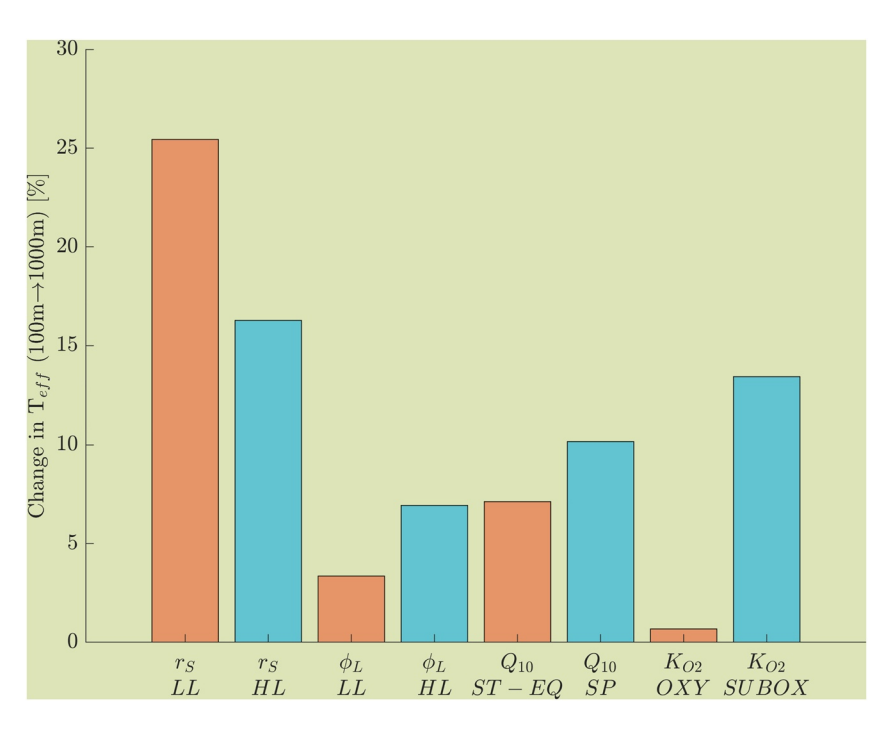


Figure 6. A regional breakdown of the $\overline{T_{\rm eff}}$ response to variations in r_s , ϕ_L , Q_{10} , and K_{02} . The vertical extent of each bar represents the change in $\overline{T_{\rm eff}}$ output resulting from varying a particular input parameter from its minimum value to its maximum value, while keeping all others fixed. LL stands for low latitude, HL for high latitude, ST-EQ for subtropical and equatorial regions, SP for subpolar regions, OXY for well-oxygenated regions, and SUBOX for suboxic regions (see Section 3.2.2.2 for more details). Model output is based on the standard configuration of the MSPACMAM.

A first-order Taylor series approximation is used to estimate the variance of $\overline{T_{\rm eff}}$ associated with parameter uncertainties (Equation 15). The estimated standard deviation of $\overline{T_{\rm eff}}$ is $\pm 10.7\%$ for the std configuration and $\pm 13.0\%$ for the frag configuration. r_S makes the largest contribution of 52.51% to the estimated $\overline{T_{\rm eff}}$ variance. $k_{\rm POC}$ also contributes substantially to the $\overline{T_{\rm eff}}$ variance, accounting for 35.55%. The percentage contributions from Q_{10} , K_{O_2} , and ϕ_L to the variance of $\overline{T_{\rm eff}}$ are relatively small. Q_{10} and K_{O_2} make similar contributions of 5.04% and 4.65%, respectively, while ϕ_L contributes only 2.25%. It is interesting to note that while ϕ_L contributes least to the estimated variance of $\overline{T_{\rm eff}}$, it is the model parameter to which $\overline{T_{\rm eff}}$ is most sensitive (in terms of the normalized sensitivity coefficients). This demonstrates that a sensitive parameter is not necessarily important for the output variance if the parameter's reasonable range (defined here as its literature-based variance) is relatively small as is the case for ϕ_L .

3.2.2.2. Regional Differences in the Sensitivity of Transfer Efficiency

In this section, we will use $\overline{T_{\rm eff}}$ to denote the model's $T_{\rm eff}$ response averaged over a specific biogeographical region. Figure 6 shows a regional breakdown of the changes in $\overline{T_{\rm eff}}$ output in response to perturbed values of r_s , ϕ_L , Q_{10} , and K_{O_2} . Variations in r_s have a larger impact on $\overline{T_{\rm eff}}$ at low latitudes (i.e., in regions equatorward of 45°) than at high latitudes (i.e., in regions poleward of 45°), whereas the opposite is the case for ϕ_L . r_s accounts for 55.3% of the estimated $\overline{T_{\rm eff}}$ variance at low latitudes and 38.9% at high latitudes, while ϕ_L contributes 8.9% at high latitudes and 1.19% at low latitudes. Figure 7 demonstrates that large particles contribute more to the bulk sinking POC flux in the high-latitude regions than at low latitudes, whereas the contribution from small particles to the total POC flux is larger at low latitudes than in the high-latitude regions (see Figure C1). As a result, the $\overline{T_{\rm eff}}$ output at high latitudes is more sensitive to assumptions about ϕ_L and less sensitive to those about r_s , and vice versa for the low-latitude regions.

The most striking regional difference in the $\overline{T_{\rm eff}}$ response is its much larger sensitivity to K_{O_2} in oxygen-deficient waters than in well-oxygenated waters. K_{O_2} contributes 12.25% to the estimated variance of $\overline{T_{\rm eff}}$ in suboxic regions (defined here as waters where $[O_2]$ is < 5 mmol m⁻³), compared to only 0.08% in high-oxygen regions

DINAUER ET AL. 16 of 34

19449224, 2022, 10, Downloaded from https://agupubs.onlinelibrary.wiley.com/doi/10.1029/20.21GB007131, Wiley Online Library on [18/11/2024]. See the Terms and Conditions (https://onlinelibrary.wiley.com/term

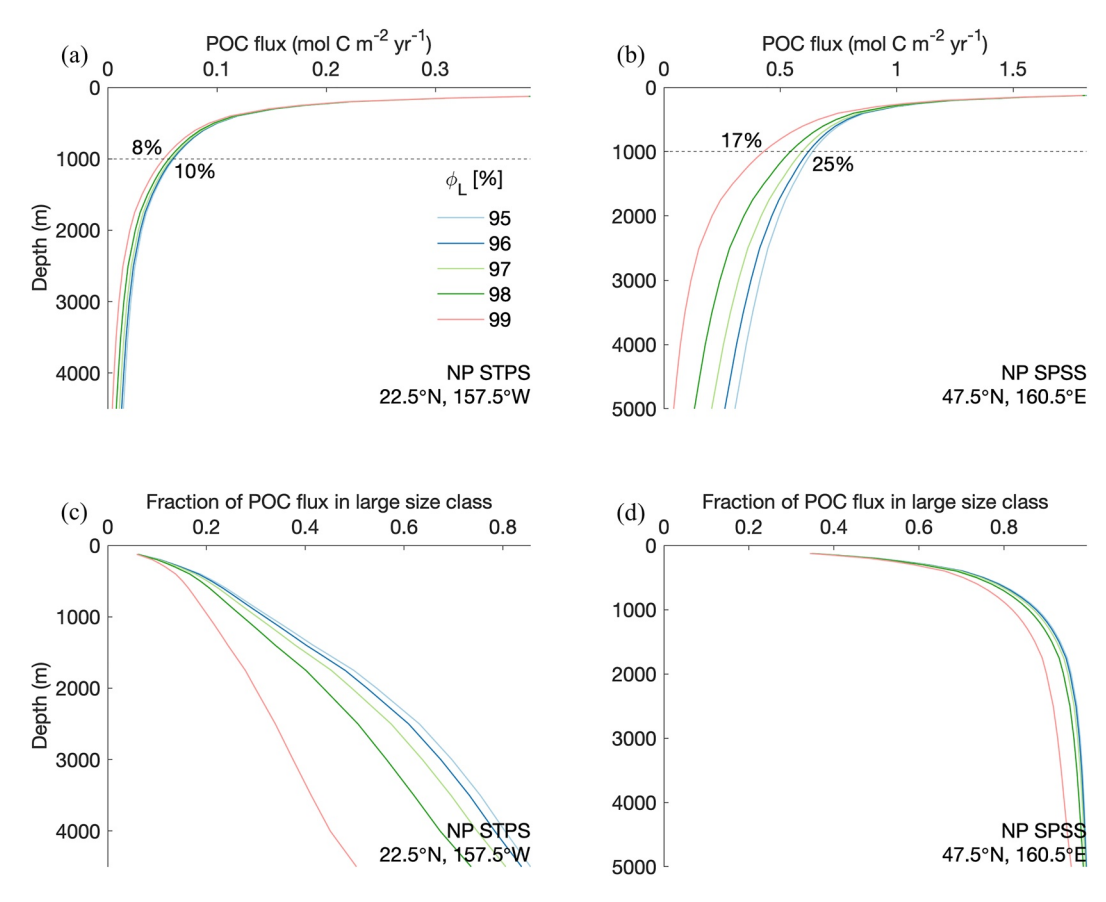


Figure 7. A comparison of vertical POC flux attenuation for two locations exemplary of the regional character of ϕ_L sensitivity: the low-latitude North Pacific (left) and the high-latitude Northwest Pacific (right). The *upper panels* (a, b) show the POC flux profile resulting from varying ϕ_L over its literature-based range at each location. The flux profiles are annotated with the corresponding range of $T_{\rm eff}$ values. In the *lower panels* (c, d), vertical profiles of the fractional contribution from large particles to the bulk sinking POC flux are shown at the two locations. Model results are based on the standard configuration of the MSPACMAM.

(defined here as waters where $[O_2]$ is > 100 mmol m⁻³). This localized sensitivity suggests that the actual value of K_{O_2} is not critical on a global scale, unless the threshold oxygen concentration at which anaerobic respiration begins is assumed to be very high (e.g., $K_{O_2} = 100 \text{ mmol m}^{-3}$). The specification of the value of K_{O_2} , however, is crucial for the ocean's most-oxygen-depleted oxygen minimum zone regions, i.e., at oxygen concentrations less than 5 mmol m⁻³. As an example, Figure 8 compares the response of the POC flux profile to changes in K_{O_2} at two locations: one in the oxygen minimum zone of the Eastern Tropical North Pacific and the other in the high-oxygen waters of the high-latitude North Atlantic. Variations in K_{O_2} have no influence on T_{eff} values in the oxygenated water column of the North Atlantic, whereas T_{eff} values vary considerably in the suboxic layer of the water column in the Eastern Tropical North Pacific.

Different temperature regimes are expected to exhibit varying degrees of Q_{10} sensitivity. Interestingly, the regional breakdown provided in Figure 6 shows that the $\overline{T_{\rm eff}}$ output is more sensitive to variations in Q_{10} in cold, high-latitude regions (defined here as seasonally stratified subpolar regions north of 45°N or south of 45°S) than in the warmer mid-latitudes and tropics (defined here as permanently stratified subtropical regions and equatorial regions). Q_{10} contributes 12.47% to the estimated $\overline{T_{\rm eff}}$ variance in subpolar regions, compared to 3.60% in thermally stratified regions. For subtropical and equatorial regions with a sharp vertical temperature gradient, the positive effect of increasing Q_{10} on remineralization rates in warm surface waters is counteracted by the opposite effect at deeper depths where cold waters predominate, leading to a dampening of POC flux attenuation over the top ~1,000 m. In contrast, when Q_{10} is increased at high-latitude locations, the rate of remineralization is decreased everywhere in the vertical since high-latitude water columns tend to be uniformly cold. As an example, the response of the POC

DINAUER ET AL. 17 of 34

9449224, 2022, 10, Downloaded from https://agupubs.onlinelibrary.wiley.com/doi/10.1029/2021GB007131, Wiley Online Library on [18/11/2024]. See the Terms and Conditions (https://onlinelibrary.wiley.com/doi/10.1029/2021GB007131, Wiley Online Library on [18/11/2024]. See the Terms and Conditions (https://onlinelibrary.wiley.com/doi/10.1029/2021GB007131, Wiley Online Library on [18/11/2024]. See the Terms and Conditions (https://onlinelibrary.wiley.com/doi/10.1029/2021GB007131, Wiley Online Library on [18/11/2024]. See the Terms and Conditions (https://onlinelibrary.wiley.com/doi/10.1029/2021GB007131, Wiley Online Library on [18/11/2024]. See the Terms and Conditions (https://onlinelibrary.wiley.com/doi/10.1029/2021GB007131, Wiley Online Library on [18/11/2024]. See the Terms and Conditions (https://onlinelibrary.wiley.com/doi/10.1029/2021GB007131, Wiley Online Library on [18/11/2024]. See the Terms and Conditions (https://onlinelibrary.wiley.com/doi/10.1029/2021GB007131, Wiley Online Library on [18/11/2024]. See the Terms and Conditions (https://onlinelibrary.wiley.com/doi/10.1029/2021GB007131, Wiley Online Library on [18/11/2024]. See the Terms and Conditions (https://onlinelibrary.wiley.com/doi/10.1029/2021GB007131, Wiley Online Library on [18/11/2024]. See the Terms and Conditions (https://onlinelibrary.wiley.com/doi/10.1029/2021GB007131, Wiley Online Library on [18/11/2024]. See the Terms and Conditions (https://onlinelibrary.wiley.com/doi/10.1029/2021GB007131, Wiley Online Library on [18/11/2024]. See the Terms and Conditions (https://onlinelibrary.wiley.com/doi/10.1029/2021GB007131, Wiley Online Library.wiley.com/doi/10.1029/2021GB007131, Wiley Online Library.wiley.com/doi

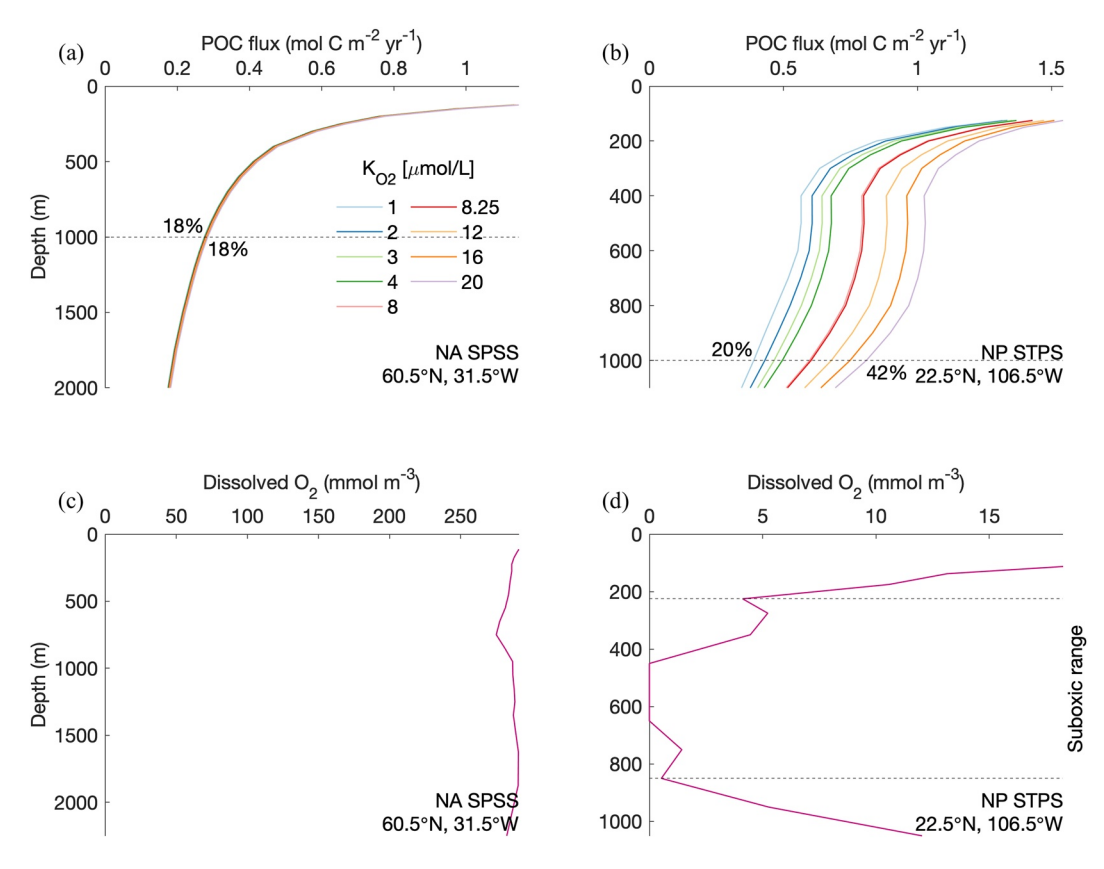


Figure 8. A comparison of vertical POC flux attenuation for two locations exemplary of the regional character of K_{O_2} sensitivity: the high-latitude North Atlantic (left) and the Eastern Tropical North Pacific oxygen minimum zone (right). The *upper panels* (a, b) show the POC flux profile resulting from varying K_{O_2} over its literature-based range at each location. The flux profiles are annotated with the corresponding range of T_{eff} values. Model results are based on the standard configuration of the MSPACMAM. In the *lower panels* (c, d), vertical profiles of dissolved oxygen are shown at the two locations. The pair of dashed black lines delineates the suboxic layer, where $[O_2]$ is < 5 mmol m⁻³.

flux profile to variations in Q_{10} is shown in Figure 9 for two locations belonging to different temperature regimes. The range of $T_{\rm eff}$ values is considerably larger in the Northwest Pacific subarctic gyre than in the North Pacific subtropical gyre, reflecting differences in the steepness of their vertical temperature gradients.

3.3. Spatial Variability in Mesopelagic Transfer Efficiency

3.3.1. Global Pattern of Transfer Efficiency

Figure 10 shows the global distribution of $T_{\rm eff}$ from the ctrl simulation for model configurations std and frag. Under both configurations, the model simulates a spatial pattern of $T_{\rm eff}$ that is latitudinal in character with a north–south $T_{\rm eff}$ gradient in both hemispheres. Values of $T_{\rm eff}$ are generally larger at high latitudes (18.5 \pm 3.76%) than at low latitudes (11.7 \pm 2.47%), although there are a few exceptions to this, including high $T_{\rm eff}$ values in the equatorial Eastern Tropical Pacific. The spread in $T_{\rm eff}$ values for the std configuration is similar to that for the frag configuration. The 5th and 95th percentiles of the $T_{\rm eff}$ values for the std configuration are 8.63% and 21.9%, a spread which is only slightly higher than the 9.41% to 20.8% range for the frag configuration. However, the spatial variance of $T_{\rm eff}$ is noticeably smaller for the frag configuration (14.8) than for the std configuration (20.5). This is because the inclusion of large particle fragmentation in the model under the frag configuration acts to reduce the latitudinal gradient in particle size initially established at the surface, leading to a relatively more homogenous pattern of $T_{\rm eff}$ compared to the std configuration.

The spatial pattern of $T_{\rm eff}$ simulated by the MSPACMAM agrees well with recent model simulations from Weber et al. (2016) (data-constrained ocean circulation inverse model), DeVries and Weber (2017) (data-assimilated model of the biological pump), Cram et al. (2018) (mechanistic sinking particle flux model), and Maerz

DINAUER ET AL. 18 of 34

9449224, 2022, 10, Downloaded from https://agupubs.onlinelibrary.wiley.com/doi/10.1029/2021GB007131, Wiley Online Library on [18/11/2024]. See the Terms and Conditions (https://onlinelibrary.wiley.com/

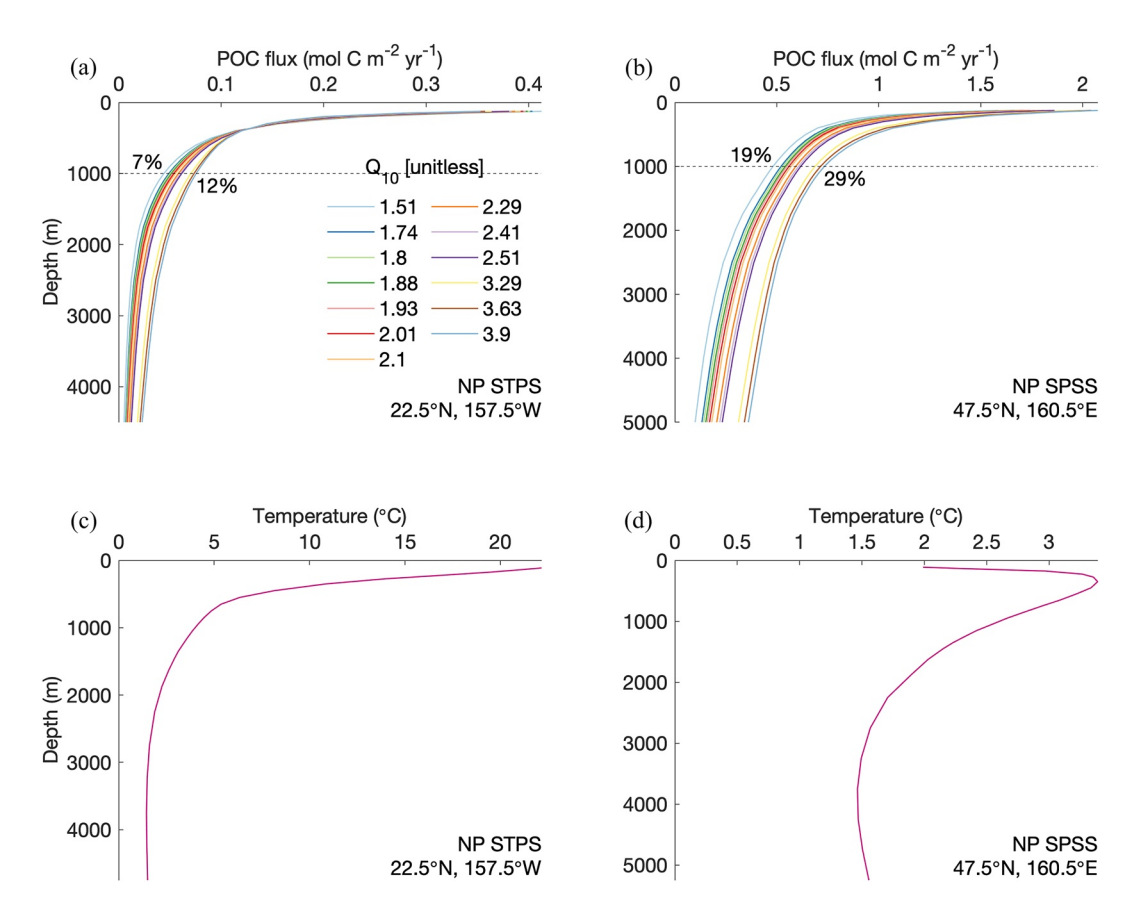


Figure 9. A comparison of vertical POC flux attenuation for two locations exemplary of the regional character of Q_{10} sensitivity: the North Pacific subtropical gyre (left) and the Northwest Pacific subarctic gyre (right). The *upper panels* (a, b) show the POC flux profile resulting from varying Q_{10} over its literature-based range at each location. The flux profiles are annotated with the corresponding range of $T_{\rm eff}$ values. Model results are based on the standard configuration of the MSPACMAM. In the *lower panels* (c, d), vertical profiles of temperature are shown at the two locations.

et al. (2020) (marine aggregate sinking scheme deployed in an ESM). Although differences in the fine structure are apparent, the main large-scale features of $T_{\rm eff}$ simulated by the five models are generally similar. All models predict a latitudinal asymmetry of $T_{\rm eff}$ with unanimous agreement on the trend of larger $T_{\rm eff}$ values in high-latitude regions than in low-latitude regions. The simulated $T_{\rm eff}$ values are typically largest in the Southern Ocean and smallest in the subtropical gyres at low latitudes and mid-latitudes. The various model $T_{\rm eff}$ ranges are qualitatively similar. It is noteworthy that the empirical model from Henson et al. (2012) simulates a very different $T_{\rm eff}$ pattern, with the largest $T_{\rm eff}$ values at low latitudes. Based on the good agreement among five structurally different models, it appears the spatial structure of the $T_{\rm eff}$ pattern is well simulated by the MSPACMAM, especially at broad spatial scales.

3.3.2. Environmental Drivers of Spatial Variations in Transfer Efficiency

The spatial pattern of $T_{\rm eff}$ has contributions from several environmental factors $EF = (EF_1, ..., EF_n)$, including ocean temperature, dissolved oxygen, seawater density, seawater viscosity, particle size, and particle density. The focus of this section is primarily on the environmental factors whose spatial variability has a significant impact on the large-scale pattern of $T_{\rm eff}$. A chi-square variance test shows that the predicted spatial pattern of $T_{\rm eff}$ from the $\overline{\rho_{\rm sw}}$ experiment (see Table 3) is statistically indistinguishable from the $T_{\rm eff}$ pattern in the ctrl simulation. Hence, the impact of seawater density on large-scale $T_{\rm eff}$ will not be discussed further. One important caveat to this analysis is that the relative importance of environmental factors in the spatial pattern of $T_{\rm eff}$ is sensitive to the assumptions underlying the model. The results of the analysis will depend on model structure and formulations, the choice of parameter values and the surface boundary fluxes used to force the model. In this work, the POC, calcite, aragonite and opal export flux fields are each constructed from a CMIP multi-model ensemble median. Exploring the sensitivity of model output to alternative particle export flux fields will be the focus of future work.

DINAUER ET AL. 19 of 34

9449224, 2022, 10, Downloaded from https://agupubs.onlinelibrary.wiley.com/doi/10.1029/2021GB007131, Wiley Online Library on [18/11/2024]. See the Terms and Conditions (https://onlinelibrary.wiley.com/terms-and-conditions) on Wiley Online Library

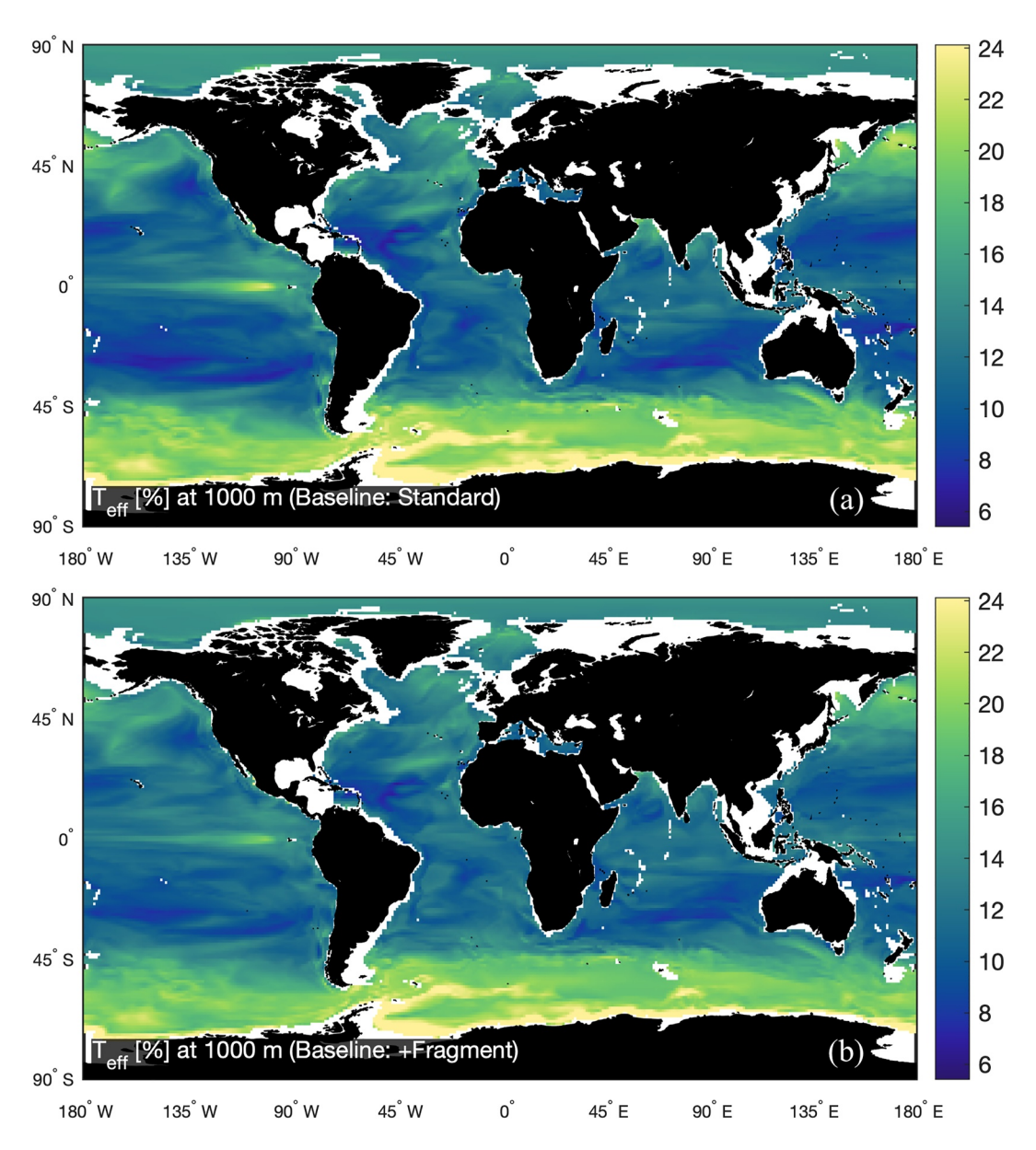


Figure 10. Global distribution of $T_{\rm eff}$ from the baseline model simulation for two different configurations. (a) Spatial pattern of $T_{\rm eff}$ simulated by the standard configuration of the MSPACMAM. (b) Spatial pattern of $T_{\rm eff}$ simulated by the model configuration including large particle fragmentation.

Figure 11 shows maps of the various environmental components of the spatial pattern of $T_{\rm eff}$ generated by the std configuration. A positive value of $\Delta T_{\rm eff}^{EF_i}$ for a particular location indicates that $T_{\rm eff}$ is larger than the global mean $T_{\rm eff}$ due to spatial variability in EF_i, while a negative value means $T_{\rm eff}$ is smaller than the mean due to space-varying EF_i. Here, we identify the environmental factors associated with the largest positive and negative $\Delta T_{\rm eff}^{EF_i}$ values, as characterized by the 5th and 95th percentiles of the $\Delta T_{\rm eff}^{EF_i}$ maps. Particle size ($\Delta T_{\rm eff}^{\sigma_L} = 8.1\%$) and ocean temperature ($\Delta T_{\rm eff}^T = 3.1\%$) have the largest positive impacts on $T_{\rm eff}$ whereas variations in particle density ($\Delta T_{\rm eff}^{\rho_{\rm EM}} = -5.1\%$) and size ($\Delta T_{\rm eff}^{\sigma_L} = -4.4\%$) induce the largest negative $T_{\rm eff}$ changes. Interestingly, particle size is less influential in the frag configuration (not shown in Figure 11). When fragmentation is included in the model, ocean temperature ($\Delta T_{\rm eff}^T = 5.9\%$) has the largest positive impact on $T_{\rm eff}$ followed by particle size ($\Delta T_{\rm eff}^{\sigma_L} = 4.8\%$), whereas particle density ($\Delta T_{\rm eff}^{\rho_{\rm EM}} = -5.6\%$), seawater viscosity ($\Delta T_{\rm eff}^{\rm visc} = -3.2\%$) and ocean temperature ($\Delta T_{\rm eff}^T = -3.1\%$) are the environmental factors with the largest negative impacts on $T_{\rm eff}$. The less important role for particle size can be explained by a tendency for large particle fragmentation to reduce the

DINAUER ET AL. 20 of 34

19449224, 2022, 10, Downloaded from https://agupubs.onlinelibrary.wiley.com/doi/10.1029/2021/GB007131, Wiley Online Library on [18/11/2024]. See the Terms and Conditions (https://onlinelibrary.wiley.com/terms-and-conditions) on Wiley Online Library for rules of use. OA article

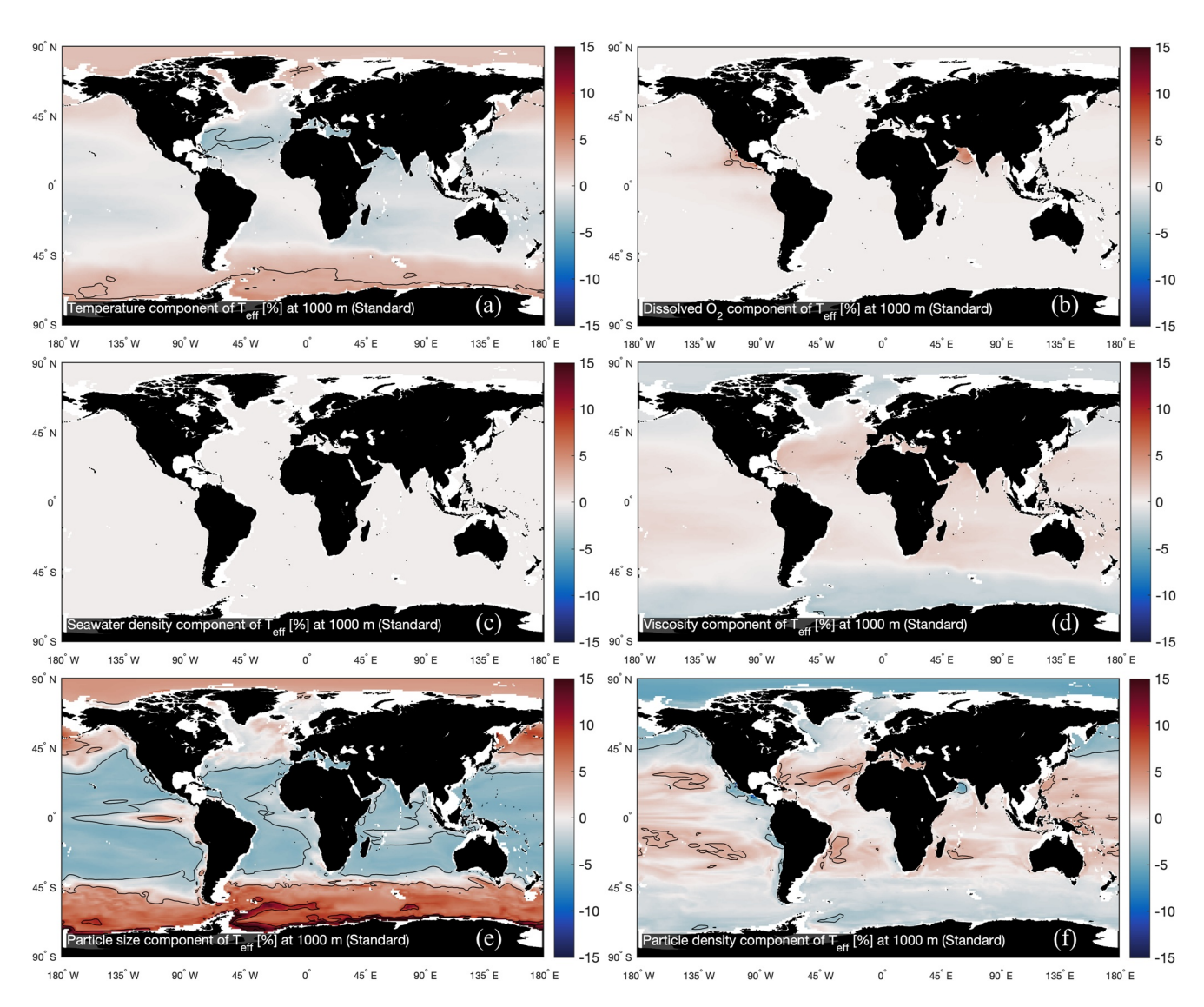


Figure 11. The predicted spatial pattern of $T_{\rm eff}$ deconvolved into individual contributions from six key environmental factors. The method of diagnosing each factor's contribution to the global $T_{\rm eff}$ variability is described in Section 2.3.2. Model results are based on the standard configuration of the MSPACMAM. The relative importance of (a) ocean temperature, (b) dissolved oxygen, (c) seawater density, (d) seawater viscosity, (e) particle size, and (f) particle density to global $T_{\rm eff}$ variability.

latitudinal gradient in particle size, initially established in the surface ocean, over the global ocean's mesopelagic zone. As large particles fragment into smaller ones as they settle through the water column, the sinking particle pool becomes mostly dominated by small particles everywhere in the horizontal and thus particle size variability becomes less important for large-scale $T_{\rm eff}$.

While the majority of $\Delta T_{\rm eff}^{\rm EF_i}$ patterns exhibit broad latitudinal structures, there exists disagreement on the sign of $\Delta T_{\rm eff}^{\rm EF_i}$ over low versus high latitudes. Particle size has a positive impact on $T_{\rm eff}$ at high latitudes and a negative impact at low latitudes. This can be explained by the fact that the opal-dominated high latitudes exhibit the greatest fractions of POC export going into large, rapidly sinking particles, resulting in enhanced vertical POC transfer. Ocean temperature also induces positive changes in $T_{\rm eff}$ at high latitudes and negative $T_{\rm eff}$ changes at low latitudes. The positive impact of temperature on $T_{\rm eff}$ in cold, high-latitude regions is consistent with the rate of chemical reactions decreasing with decreasing temperature, following the classical Arrhenius equation. In contrast to particle size and ocean temperature, both particle density and seawater viscosity have a positive impact on $T_{\rm eff}$ in low-latitude regions and a negative impact in high-latitude regions. The positive impact of particle density on $T_{\rm eff}$ at low latitudes can be explained by the presence of denser ballast minerals (i.e., CaCO₃) that act to increase bulk particle sinking speeds. Seawater viscosity positively affects $T_{\rm eff}$ at low latitudes since sinking particles encounter

DINAUER ET AL. 21 of 34

9449224, 2022, 10, Downloaded from https://agupubs.onlinelibrary.wiley.com/doi/10.1029/2021GB007131, Wiley Online Library on [18/11/2024]. See the Terms

Table 7Statistical Measures of the Relative Importance of Each Environmental Factor, EF_p in the Spatial Pattern of $T_{\rm eff}$

Environmental factor	$\begin{array}{c} \text{SD of} \\ \Delta T_{\text{eff}}^{EF_i} \\ (\%) \end{array}$	Ratio of SD of $\Delta T_{\mathrm{eff}}^{EF_{i}}$ to SD of $T_{\mathrm{eff}}^{\mathrm{ctrl}}$	RMSE between $T_{\rm eff}^{\rm ctrl}$ and $T_{\rm eff}^{\overline{EF_i}}$ (%)	Factor importance	
		Standard configuration			
Temperature	1.70	0.37	1.74	0.37	
Oxygen	0.41	0.09	0.43	0.09	
Seawater density	0.01	0.002	0.01	0.002	
Viscosity	1.14	0.25	1.14	0.24	
Particle size	4.70	1.04	4.72	1.00	
Particle density	2.31	0.51	2.35	0.50	
		Configuration	with fragmentatio	n	
Temperature	3.11	0.81	3.23	1.00	
Oxygen	0.28	0.07	0.29	0.09	
Seawater density	0.02	0.005	0.02	0.006	
Viscosity	1.71	0.44	1.74	0.54	
Particle size	2.63	0.68	2.66	0.83	
Particle density	2.33	0.61	2.37	0.73	

Note. Rows and columns represent individual factors and measures, respectively. $T_{\rm eff}^{ctrl}$ is the spatial pattern of $T_{\rm eff}$ from the baseline model simulation in which all factors vary spatially. $T_{\rm eff}^{EF_l}$ is the spatial pattern of $T_{\rm eff}$ from a model experiment in which EF_i is forced to be spatially uniform (i.e., its spatial variability has been removed). $\Delta T_{\rm eff}^{EF_l}$ is the component of the spatial pattern of $T_{\rm eff}$ attributable to space-varying EF_i , calculated as the difference between the $T_{\rm eff}^{ctrl}$ and $T_{\rm eff}^{EF_l}$ patterns. The standard deviation SD of the global $\Delta T_{\rm eff}^{EF_l}$ pattern is shown in the second column. The ratio of the standard deviations of $\Delta T_{\rm eff}^{EF_l}$ to $T_{\rm eff}^{ctrl}$ (third column) reveals whether the two patterns have similar amplitudes of variability. Shown in the fourth column is the RMSE between $T_{\rm eff}^{ctrl}$ and $T_{\rm eff}^{EF_l}$, which is the root-mean-square error occurring when spatial variations in EF_i have been neglected. This measure of importance is used to determine the factor importance index (fifth column), defined as the factor's RMSE divided by the maximum RMSE of all factors.

a smaller viscous resistance from the warm, low-latitude water flowing past them, resulting in faster bulk particle sinking speeds. The impact of dissolved oxygen on $T_{\rm eff}$ is apparent only over the largest and most-oxygen-depleted oxygen minimum zones in the Eastern Tropical Pacific and the Arabian Sea, where very low oxygen concentrations decrease the POC remineralization rate and therefore increase $T_{\rm eff}$.

A few simple statistical measures are used to determine the relative importance of each environmental factor to global $T_{\rm eff}$ variability (see Table 7). One measure of factor importance involves calculating the root-mean-square error (RMSE) between $T_{\rm eff}^{\rm ctrl}$ and $T_{\rm eff}^{\overline{\rm EF}_i}$, which may be thought of as the error occurring when spatial variations in factor EF, are not considered. The errors obtained in this fashion are utilized to calculate a "factor importance index" (FI), which is equal to the RMSE for EF, divided by the greatest RMSE among all environmental factors $EF = (EF_1, \dots, EF_n)$. Particle size, particle density, and ocean temperature emerge as the most important determinants of global $T_{\rm eff}$ variability. For the std configuration, the spatial variability in $T_{\rm eff}$ can be attributed largely to the contribution from particle size variability (FI = 1.0) and in smaller part to particle density (FI = 0.50) and ocean temperature (FI = 0.37). For the frag configuration, the spatial pattern of $T_{\rm eff}$ is attributable in more equal measure to contributions from ocean temperature (FI = 1.0), particle size (FI = 0.83), and particle density (FI = 0.73). The error originating from the removal of spatial variability in seawater viscosity is nontrivial, especially for the frag configuration (FI = 0.54), whereas the errors due to neglecting variations in dissolved oxygen and seawater density are very small or negligible on a global scale. Table 7 introduces two other importance measures that both come to the same ranking of factor importance.

3.4. Basic Assumptions Underlying the Model

Although it provides a useful tool for understanding what controls large-scale $T_{\rm eff}$, the MSPACMAM makes several simplifying assumptions. The treatment of the partitioning of POC export into small and large particles has obvious simplifications. The straightforward approach used in the model assumes that the fraction of POC export entering the large size class, σ_L , is proportional to the fraction of total particle export consisting of opal and aragonite, both of which are biogenic minerals associated with large plank-

ton (i.e., diatoms and pteropods, respectively). For simplicity, the constant of proportionality, κ_L , between σ_L and the relative abundance of opal and aragonite export is assumed to be 1. There are four main reasons for the POC export partitioning scheme used in the MSPACMAM. First, most ESMs prognostically calculate POC, CaCO₃ and opal export fluxes, so the MSPACMAM modeling framework can be readily deployed in such models. Second, the use of the scheme avoids the need to employ some version of a marine ecosystem and/or particle aggregation model in the surface production zone, both of which can introduce new sources of model errors and uncertainties via additional uncertain parameters. Third, the partitioning of POC export into differently sized particles based on the relative abundance of opal and aragonite export has the advantage of being able to respond to changing forcing, specifically any forcing that affects the prognostic calculation of export production, which is not the case for, e.g., a power law-based particle size distribution. Fourth, the resultant spatial pattern of σ_L (Figure A1) is consistent with global distributions of size-partitioned carbon biomass derived from the satellite-based particulate backscattering spectrum (Kostadinov et al., 2016), showing that large particles make a larger contribution in the opal-dominated high latitudes than in the CaCO₃-dominated low latitudes. Future studies may benefit from improvements in the choice of κ_L .

The model also makes an assumption about the partitioning of calcite export between small and large particles. It is straightforward to treat the fraction of calcite export consisting of large particles in the same manner as the

DINAUER ET AL. 22 of 34

fraction of POC export going into large particles. This approach was motivated in part by the results of laboratory studies, which suggest that diatom aggregates are effective at scavenging coccoliths and other small calcite particles (De La Rocha et al., 2008; Iversen & Ploug, 2010; Passow & De La Rocha, 2006). While it is sensible to assume that some fraction of calcite export participates in the large particle size class, the constant of proportionality associated with this fraction could be revisited in future work. For example, information from food web models could be combined with satellite-based phytoplankton functional type distributions to refine this constant. Another potential target for model improvement is the treatment of refractory and/or protected POC, which has been hypothesized to be associated with the particles sinking out of the surface ocean in the CaCO₃-dominated low latitudes (Henson et al., 2012).

Rubey's (1933) equation is used to calculate the sinking speeds of small and large particles, w_{sink}^S and w_{sink}^L . Since it was derived by equating the effective weight of a spherical particle to both viscous and inertial forces, Rubey's equation represents an improvement over Stokes' law of viscous resistance. Its application is suitable for the turbulent flow regime in which inertial forces dominate over viscous forces, i.e., when the particle Reynolds number Re_p is outside the Stokes' range ($Re_p > 0.5$). In contrast, Stokes' law applies only in the laminar (or viscous) flow regime where $Re_p < 0.5$. The particle settling velocities given by the two equations are similar at low Re_p but diverge for particles sinking outside the Stokes' range, with the velocities given by Rubey's equation lower than those given by Stokes' law. While a number of possibly important factors (e.g., the effects of shape and surface roughness) have been neglected in its derivation, the advantage of using Rubey's equation in the model is that it allows for the calculation of environmentally dependent, space-varying w_{sink}^S and w_{sink}^L .

The representation of the effects of zooplankton migration, such as large particle fragmentation, should be a priority target for model improvement. The MSPACMAM does not include diel and/or seasonal vertical migration of zooplankton and only implicitly represents zooplankton-mediated fragmentation by assuming that the rate constant k_{frag}^L encompasses all physical and biological processes that fragment large particles into smaller ones. While it is likely that neglecting active transport of carbon by vertically migrating zooplankton has a relatively small impact on the climatological annual mean spatial pattern of $T_{\rm eff}$ since POC export at a large spatial scale is thought to be dominated by the gravitational settling of particles (Boyd et al., 2019; Resplandy et al., 2019), recent field work has demonstrated that particle fragmentation is a key process governing POC flux attenuation in a regional context. For example, the breakup of particles by biotic and/or abiotic mechanisms may account for almost half of the observed large particle flux loss in the North Atlantic and Southern Ocean (Briggs et al., 2020), whereas the general absence of zooplankton in oxygen minimum zones contributes to the preservation of sinking POC in these regions (Cavan et al., 2017). A major innovation in the MSPACMAM would be the incorporation of mechanistic representations of fragmentation mechanisms, such as physical disaggregation by turbulence-generated shear stress (Alldredge et al., 1990) and zooplankton "sloppy feeding" (Anderson & Tang, 2010; Lampitt et al., 1990) and/or swimming behavior (Dilling & Alldredge, 2000; Goldthwait et al., 2004). However, a more complex treatment of particle fragmentation will be constrained by available observations and limited by current knowledge. Future research efforts could focus on experimental approaches and field studies in order to generate a more detailed understanding of the individual fragmentation processes and their relative importance in the net vertical transport of carbon.

3.5. Synthesis of Transfer Efficiency Sensitivity Results

In Section 3.2, we showed that reasonable changes in model parameters can significantly alter the shape of the vertical POC flux profile. Similar to Omand et al. (2020), we find that the flux profile is very sensitive to the choice of the base remineralization rate constant $k_{\rm POC}$. $T_{\rm eff}$ ranged from 11.5% to 39.0% when $k_{\rm POC}$ referenced to 20°C was varied from 0.035 to 0.32 d⁻¹. Omand et al. (2020) showed that the export efficiency (defined as export at 100 m divided by net primary production) ranged from 40% to 82% when their model's remineralization rate was varied from 0.01 to 0.16 d⁻¹. Cram et al. (2018) and Omand et al. (2020) found that the slope of the particle size distribution, which determines the proportion of small, slow-sinking particles versus large, fast-sinking particles, has a significant influence on the bulk POC flux profile. While our model structure does not rely on a power law-based particle size distribution, varying the small particle radius r_s , while holding all else constant, has the effect of varying bulk particle sinking speeds. As expected, our sensitivity analysis demonstrated that the choice of the small particle radius r_s strongly influences the bulk POC flux profile. As in Cram et al. (2018), the influence of Q_{10} on vertical POC flux attenuation varies

DINAUER ET AL. 23 of 34

9449224, 2022, 10, Downloaded from https://agupubs.onlinelibrary.wiley.com/doi/10.1029/2021GB007131, Wiley Online Library on [18/11/2024]. See the Terms and Condition

regionally between subtropical and high-latitude regions, which can be attributed to regional differences in the steepness of the vertical temperature gradient. Also consistent with the findings of Cram et al. (2018), the modeled POC flux profile is rather insensitive to the oxygen dependence of remineralization, K_{O_2} , except in suboxic regions where oxygen is effectively absent from seawater.

As highlighted by DeVries and Weber (2017), the factors controlling the spatial pattern of $T_{\rm eff}$ are the subject of active debate. In experiments with the MSPACMAM, three environmental factors emerged as the most important determinants of the spatial pattern of $T_{\rm eff}$ (see Section 3.3). The largest contributors to the simulated $T_{\rm eff}$ pattern are particle size, particle density, and ocean temperature, with the caveat that these results depend on our model structure/formulations, parameter values, and boundary conditions. The MSPACMAM predicts that vertical POC transfer is more efficient in the cold, opal-dominated high latitudes, which can be explained by the presence of large, rapidly sinking particles and the reduction in the temperature-dependent rate of remineralization, both of which compensate for the absence of dense ballast provided by CaCO₃ and the viscous resistance offered by cold waters at high latitudes. Maerz et al. (2020) reported similar results. Cram et al. (2018) have highlighted the importance of ocean temperature and particle size in the spatial pattern of $T_{\rm eff}$, whereas DeVries and Weber (2017) concluded that the general pattern of Teff is shaped by temperature and modulated by low oxygen levels. Likewise, our model results indicate that, although it contributes little to the global $T_{\rm eff}$ variability, dissolved oxygen has a strong local impact in the global ocean's three major oxygen minimum zones, i.e., the Eastern Tropical North Pacific, the Eastern Tropical South Pacific, and the Arabian Sea. Cram et al. (2018) also find that oxygen explains very little of the global $T_{\rm eff}$ variability outside oxygen minimum zones. Maerz et al. (2020) appear to overestimate the extent and intensity of $T_{\rm eff}$ in the equatorial Eastern Tropical Pacific, which may be attributed to a tendency for ESMs to overestimate the volume of oxygen minimum zones (Bopp et al., 2013; Cabré et al., 2015; Cocco et al., 2013; Kwiatkowski et al., 2020).

4. Summary and Conclusions

The spatial pattern of the mean state of $T_{\rm eff}$ simulated by the MSPACMAM is consistent with several recent model studies (Cram et al., 2018; DeVries & Weber, 2017; Maerz et al., 2020; Weber et al., 2016), showing that vertical POC transfer is more efficient at high latitudes than at low latitudes. This correspondence between five structurally different models suggests that the models correctly simulate the climatological annual mean spatial pattern of $T_{\rm eff}$. However, it is unclear whether high-latitude $T_{\rm eff}$ is higher than low-latitude $T_{\rm eff}$ on all timescales. The simulation of the seasonal cycle of $T_{\rm eff}$ requires high-quality time-series measurements of sinking POC fluxes at strategic geographical locations. The ability of models to simulate the seasonality in POC fluxes is a necessary prerequisite for improving our predictive understanding of seasonal variability in the efficiency of the ocean's biological carbon pump.

The spatial pattern of T_{eff} in a warming climate is not known. Experiments with the MSPACMAM suggest that particle properties (i.e., size and density), ocean temperature, and to a lesser extent, seawater viscosity drive most of the $T_{\rm eff}$ variability over the contemporary global ocean, whereas seawater density has a negligible influence and dissolved oxygen only a local impact. The direct effect of elevated ocean temperatures will be to enhance remineralization rates and therefore reduce $T_{\rm eff}$, whereas the smaller viscous resistance offered by warmer waters will lead to higher T_{eff}. The indirect effects of ocean warming on particle properties are more complex. Changes in the species composition (floristic shifts) and geographical distribution (faunistic shifts) of the phytoplankton community are expected to accompany climate change (Basu & Mackey, 2018; Boyd, 2015; Boyd et al., 2010; Passow & Carlson, 2012). There is a tendency for models to simulate a shift toward small-celled phytoplankton in response to climate change, along with a poleward shift in coccolithophorids in a warming ocean. However, in addition to uncertainties in future projections of phytoplankton distributions, the associated changes in the biophysical properties of sinking particles are not well established. As a consequence, it is difficult to speculate about whether changes in particle size and density under a warming climate will enhance or reduce $T_{\rm eff}$. A model such as the MSPACMAM could be deployed in ESMs in order to quantify the cumulative first-order effects of climate change on $T_{\rm eff}$. Recommendations for future modeling efforts include (a) assessing the reliability of projected future changes in the phytoplankton community structure and (b) investigating how spatial patterns of particle properties will change in response to climate change.

DINAUER ET AL. 24 of 34

19449224, 2022, 10, Dowloaded from https://gugupubs.onlinelibrary.viley.com/doi/10.1029/2021GB007131, Wiley. Online Library on [18/11/2024]. See the Terms and Conditions (https://onlinelibrary.viley.com/terms-and-conditions) on Wiley Online Library for rules of use; OA articles are governed by the applicable Creative Commons Licensia

Appendix A: Model Design

A1. Ocean State Variables

The model is run with a prescribed ocean state that is based on observed climatologies. The climatological annual mean fields from the World Ocean Atlas 2018 (WOA18; Boyer et al., 2018) define the model's temperature and dissolved oxygen variables and are used to calculate two model variables, seawater density and viscosity. The empirical correction from Bianchi et al. (2012) was applied to the dissolved oxygen data in order to address the low-oxygen biases in the WOA18. The in situ density of seawater is calculated using the Gibbs Seawater (GSW) Oceanographic Toolbox (MATLAB version 3.06, http://www.teos-10.org/) of the Thermodynamic Equation of Seawater–2010 (TEOS-10) from McDougall and Barker (2011). The dynamic viscosity of seawater is calculated using the MIT seawater properties library routines (MATLAB version 3.1.4, http://web.mit.edu/seawater/) from Sharqawy et al. (2010) and Nayar et al. (2016). Climatological annual mean fields for the saturation state of seawater with respect to calcite and aragonite are taken from the Global Ocean Data Analysis Project version 2 (GLODAPv2) data set (Olsen et al., 2016).

A2. Surface Forcing Data Set

The prescribed export fluxes of POC, calcite, aragonite, and opal are placed at the surface boundary of the model, i.e., at a depth of 100 m. The fraction of POC or calcite export that is routed to the large particle size class in the MSPACMAM (see Figure A1) is proportional to the fraction of total particle export consisting of opal and aragonite (Equation 3). Particle export fluxes are taken from the CMIP5 and CMIP6 historical simulations for 1850–2005 and 1850–2014, respectively. A multi-model ensemble median is constructed for each of the particle export flux fields from a total of seven CMIP5/CMIP6 models. The seven models are chosen because they calculate POC, CaCO₃, and opal export fluxes interactively. For models that do not explicitly represent aragonite export production, we assume the CaCO₃ export flux field contains a spatially uniform contribution from aragonite. A value of 23% is used, which is midway between measurement- and model-based estimates (Berner & Honjo, 1981; Buitenhuis et al., 2019; Fabry, 1990; Gangstø et al., 2008).

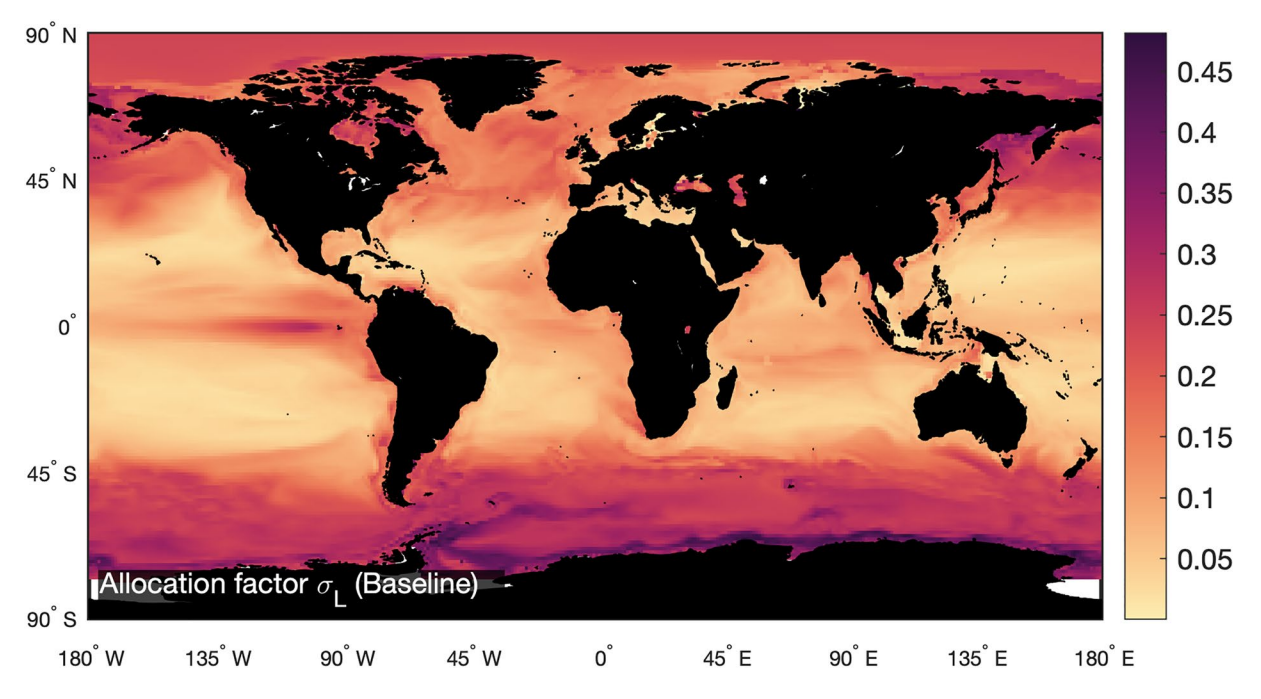


Figure A1. Global distribution of the allocation of POC export at 100 m to the large particle size class as diagnosed by the export partitioning scheme used in the MSPACMAM. The fraction of POC export going into large particles, σ_t , is assumed to be proportional to the fractional contribution of opal and aragonite to total particle export, following the classic paradigm of a diatom- and grazer-based export pathway.

DINAUER ET AL. 25 of 34

19449224, 2022, 10, Downloaded from https://agupubs.onlinelibary.wiley.com/doi/10.1029/2021GB007131, Wiley Online Library on [18/11/2024]. See the Terms and Conditions (https://onlinelibary.wiley.com/terms-and-conditions) on Wiley Online Library for rules of use; OA articles are governed by the applicable Creative Commons Licenses

The CMIP multi-model ensemble median is based on two CMIP5 (GFDL-ESM2G/TOPAZ2 and GFDL-ESM2M/TOPAZ2) and five CMIP6 (CESM2/MARBL, CNRM-ESM2-1/PISCESv2-gas, GFDL-ESM4/COBALTv2, IPSL-CM6A-LR/PISCESv2, and MPI-ESM1.2-LR/HAMOCC6) models. Although CMIP models may have a large number of ensemble members, only one member is used from each model, typically the first member (e.g., r1i1p1f1). For CMIP5 models, we use ensemble members in the "r1i1p1f" variant. For CMIP6 models, we use ensemble members in the "r1i1p1f1" or "r1i1p1f2" variant.

Appendix B: Model Evaluation

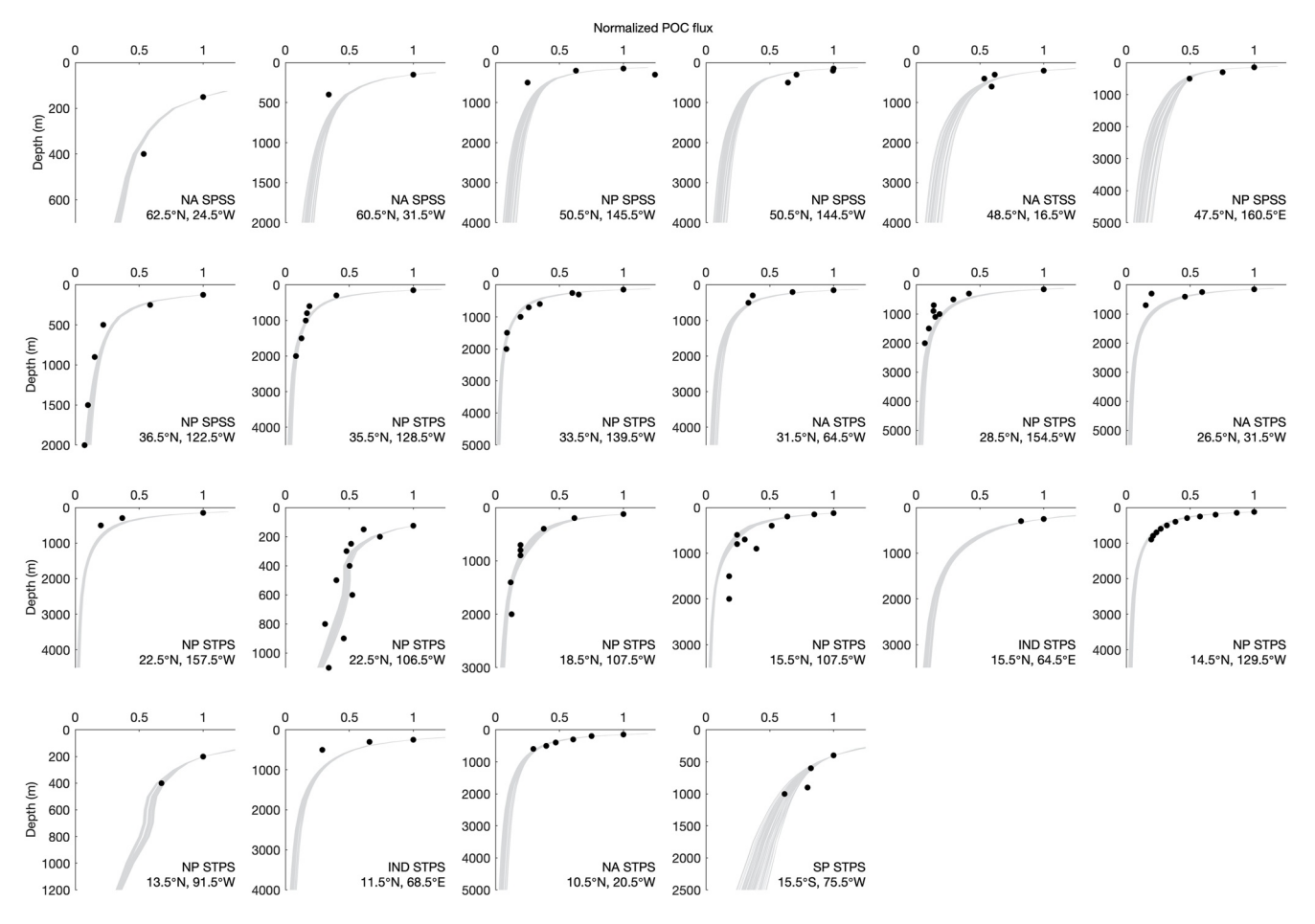


Figure B1. A comparison of modeled and observed normalized POC flux profiles at all 22 locations for which POC flux measurements are available. The thin gray lines show the individual model runs judged to be "acceptable solutions" for the standard configuration of the MSPACMAM. A total of 73 model realizations are shown. Model results are compared to observations derived either from free-drifting sediment traps or from Marine Snow Catchers (solid black circles). The vertical POC flux profiles have been normalized by their shallowest flux in order to facilitate the comparison between predictions and observations.

DINAUER ET AL. 26 of 34

19449224, 2022, 10, Downloaded from https://agupubs.onlinelibrary.wiley.com/doi/10.1029/2021GB007131, Wiley Online Library on [18/11/2024]. See the Terms and Conditions (https://onlinelibrary.wiley.com/terms-and-conditions) on Wiley Online Library for rules of use; OA articles are governed by the applicable Creative Commons Licenses

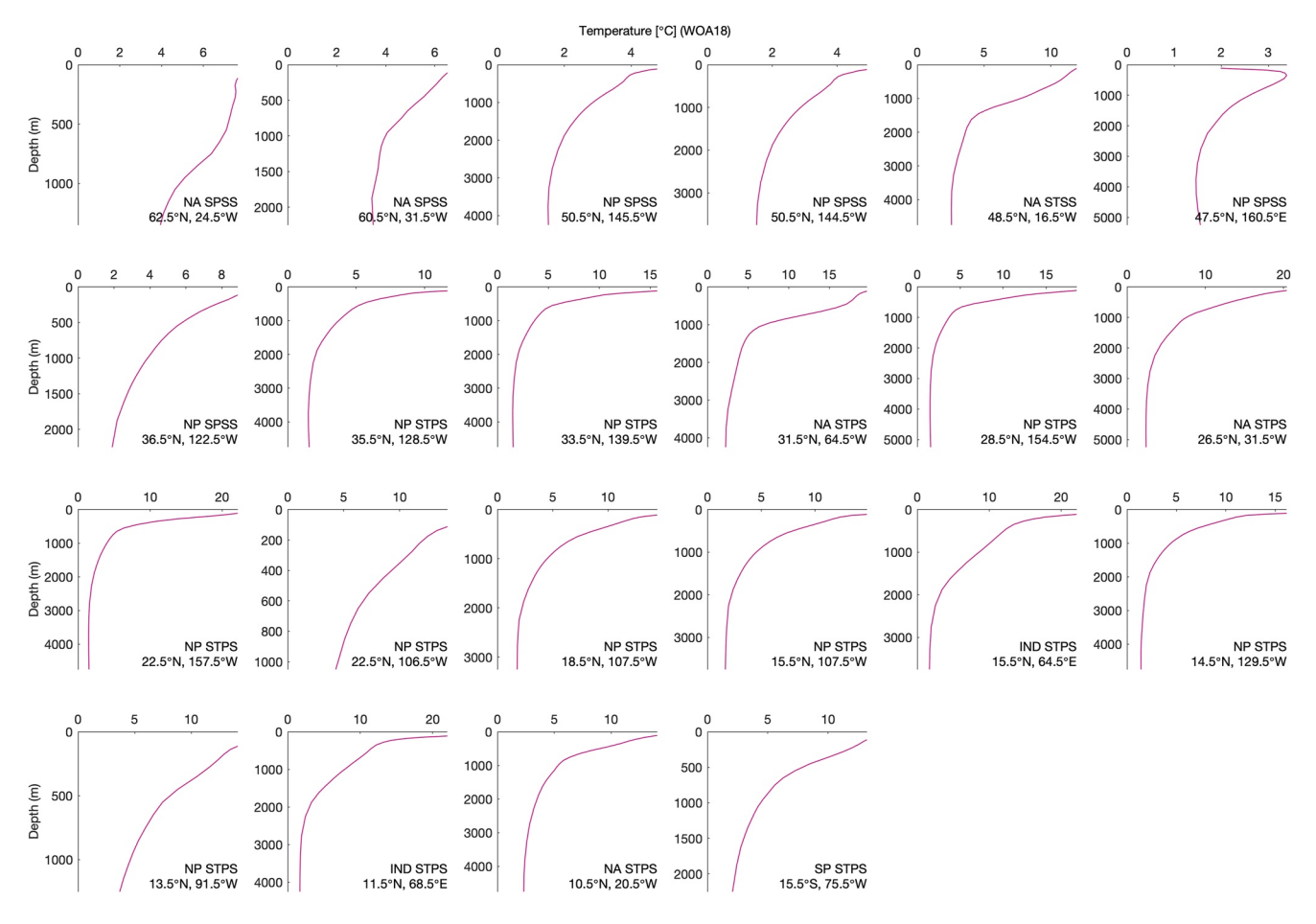


Figure B2. Vertical profiles of the observed climatological annual mean temperature at all 22 locations where POC flux measurements are available. The observed climatological values are taken from the World Ocean Atlas 2018 (WOA18).

The performance of the MSPACMAM under various parameter settings was evaluated against observed normalized sinking POC flux and log-transformed oxygen consumption rate data. Figure B1 compares the modeled and observed normalized POC flux profiles at 22 locations for which trap-derived sinking POC flux measurements were available. The data locations represented a wide range of temperature and oxygen regimes (Figure B2 and Figure B3). The model parameter combinations yielding cost function values within 5% of the minimum cost value are summarized in Table B1.

DINAUER ET AL. 27 of 34

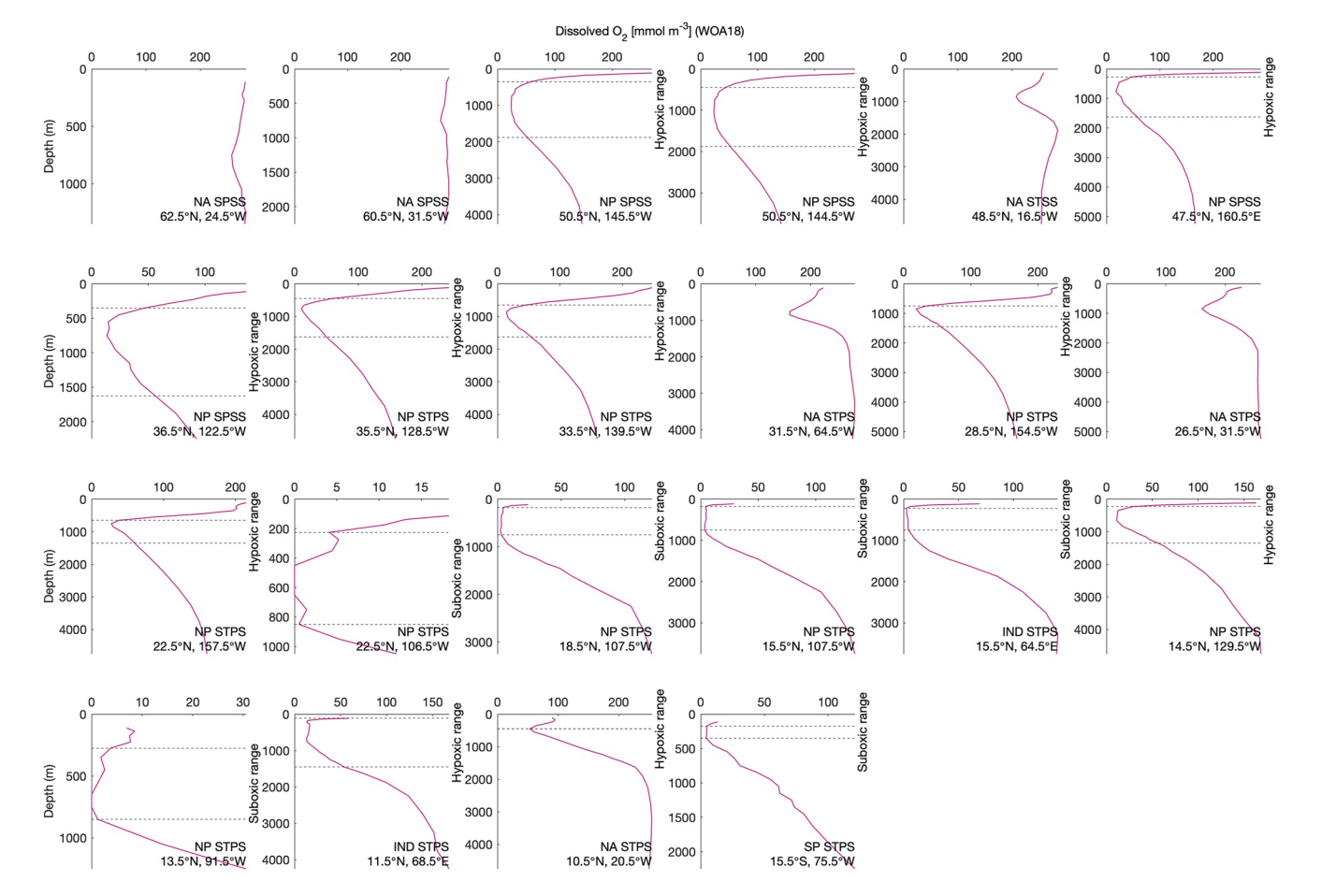


Figure B3. Vertical profiles of the observed climatological annual mean dissolved oxygen at all 22 locations where POC flux measurements are available. The observed climatological values are taken from the World Ocean Atlas 2018 (WOA18). The dashed black lines delineate hypoxic and suboxic layers. Here, the term hypoxic is used to refer to waters where $[O_2]$ is < 60 mmol m⁻³ and the term suboxic refers to waters where $[O_3]$ is < 5 mmol m⁻³.

Table B1 Ranges of the Parameter Sets Within 5% of the Minimum Cost Value						
r_S (μ m)	$\phi_L(\%)$	k_{POC}^{ref} (d ⁻¹) ^a	Q_{10} (unitless)	K_{O_2} (μ mol L ⁻¹)		
5–30	95–99	0.033-0.32	1.51-3.9	1–20		
Standard configuration ($N = 1,521$)						
10–30	95–99	0.033-0.32	1.51-2.09	1–4		
Configuration with fragmentation $(N = 1,606)$						
10–30	95–98	0.033-0.32	1.51–2.29	1–4		
	r _s (μm) 5–30 10–30	r_{S} (µm) ϕ_{L} (%) 5–30 95–99 Sta 10–30 95–99 Configur	r_S (µm) ϕ_L (%) k_{POC}^{ref} (d ⁻¹) ^a 5-30 95-99 0.033-0.32 Standard configuration (N 10-30 95-99 0.033-0.32 Configuration with fragmentat	r_S (μm) ϕ_L (%) k_{POC}^{ref} (d ⁻¹) ^a Q_{10} (unitless) 5–30 95–99 0.033–0.32 1.51–3.9 Standard configuration ($N = 1,521$) 10–30 95–99 0.033–0.32 1.51–2.09 Configuration with fragmentation ($N = 1,606$)		

^aThe POC remineralization rate constant, $k_{\rm POC}$, referenced to 20°C. Since the original, literature-based $k_{\rm POC}$ values are referenced to various temperatures $T_{\rm ref}$ (see Table 2), they have been normalized to a common reference temperature of 20°C by multiplying by $e^{b_T(20-T_{\rm ref})}$ where $b_T = \ln Q_{10}/10$. For $k_{\rm POC}$ in the model parameter sets, the accompanying Q_{10} value is used. For the a priori literature-based values of $k_{\rm POC}$, a Q_{10} value of 1.51 is used.

DINAUER ET AL. 28 of 34

19449224, 2022, 10, Downloaded from https://agupubs.onlinelibary.wiley.com/doi/10.1029/2021GB007131, Wiley Online Library on [18/11/2024]. See the Terms and Conditions (https://onlinelibary.wiley.com/terms-and-conditions) on Wiley Online Library for rules of use; OA articles are governed by the applicable Creative Commons Licenses

Appendix C: Regional Sensitivity Analysis

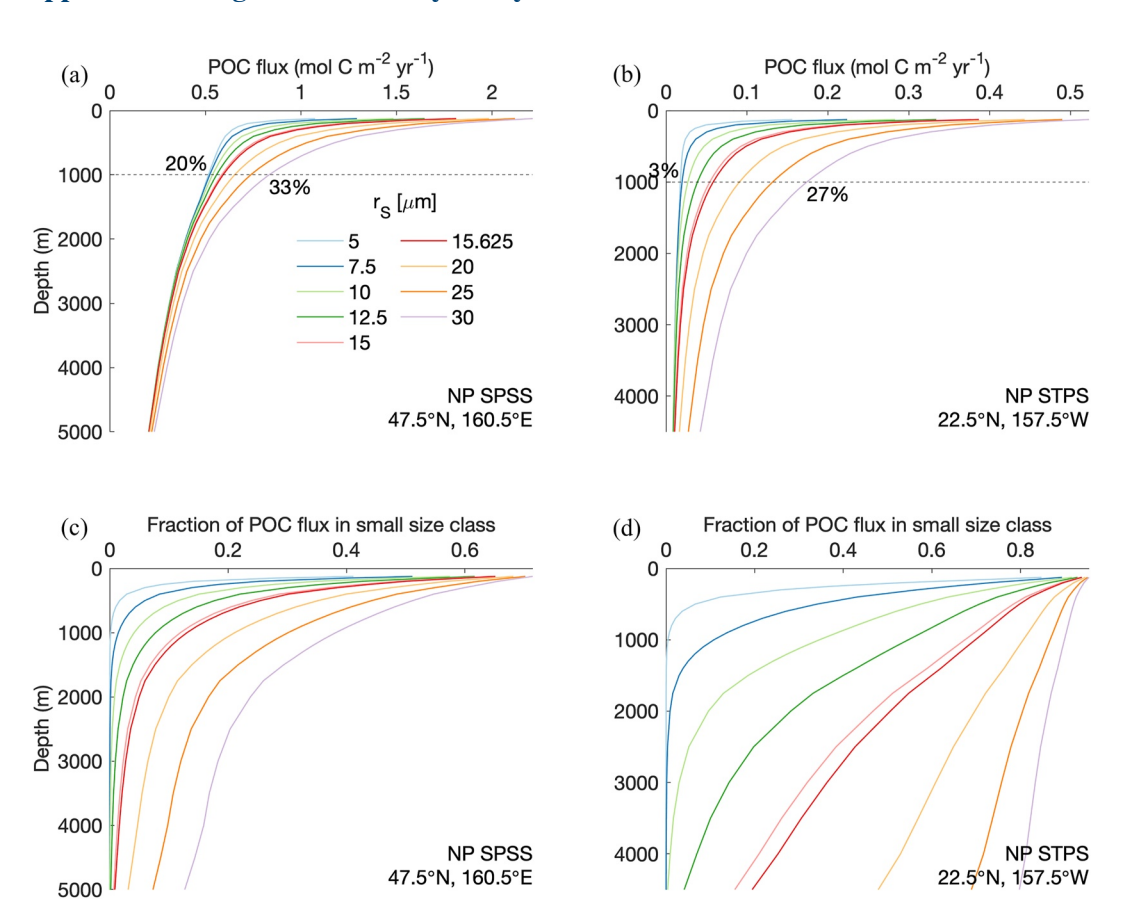


Figure C1. A comparison of vertical POC flux attenuation for two locations exemplary of the regional character of r_S sensitivity: the high-latitude Northwest Pacific (left) and the low-latitude North Pacific (right). The *upper panels* (a, b) show the POC flux profile resulting from varying r_S over its literature-based range at each location. The flux profiles are annotated with the corresponding range of $T_{\rm eff}$ values. In the *lower panels* (c, d), vertical profiles of the fractional contribution from small particles to the bulk sinking POC flux are shown at the two locations. Model results are based on the standard configuration of the MSPACMAM.

A regional sensitivity analysis is conducted to assess how the modeled POC flux profile shape responds to changes in the small particle radius at high versus low latitudes. Figure C1 demonstrates that, because small particles contribute more to the bulk sinking POC flux at low latitudes than at high latitudes, the response of the POC flux profile is more sensitive to variations in the small particle radius in low-latitude regions than in high-latitude regions.

Data Availability Statement

The compiled, processed sinking POC flux data used for model evaluation in this study are publicly available at the Zenodo repository (https://doi.org/10.5281/zenodo.6341859) licensed under the MIT License (Dinauer, 2022a). The raw POC flux data are available in the original studies cited in Section 2.2.3.1 and the References section. The MSPACMAM used to produce model output data is described thoroughly in Section 2.1 and made available in a public repository on GitHub (https://github.com/ashdinodr/mspacmam) licensed under the terms of the Apache License 2.0. The global-scale model simulation data in netCDF format are archived in the Zenodo repository (https://doi.org/10.5281/zenodo.6342033) licensed under the MIT License (Dinauer, 2022b).

DINAUER ET AL. 29 of 34

Acknowledgments

This work was made possible by the Swiss National Science Foundation (#200020_172476 and #200020_200511), the UniBE international 2021 fellowship program of the University of Bern, and the U.S. National Science Foundation Ocean Sciences Postdoctoral Research Fellowship (OCE-PRF) (NSF 2126514). C.L. acknowledges support from the Swiss National Science Foundation under grant No. 174124. F.J. acknowledges support from the European Union's Horizon 2020 research and innovation programme under grant agreement No. 820989 (project COMFORT). S.C.D. acknowledges support from the U.S. National Science Foundation via the Center for Chemical Currencies of a Microbial Planet (NSF 2019589). The work reflects only the authors' view; the European Commission and their executive agency are not responsible for any use that may be made of the information the work contains. Model simulations were performed on UBELIX (http://www. id.unibe.ch/hpc), the HPC cluster at the University of Bern.

References

- Alldredge, A. L., & Gotschalk, C. (1988). In situ settling behavior of marine snow. Limnology & Oceanography, 33(3), 339–351. https://doi.org/10.4319/lo.1988.33.3.0339
- Alldredge, A. L., Granata, T. C., Gotschalk, C. C., & Dickey, T. D. (1990). The physical strength of marine snow and its implications for particle disaggregation in the ocean. *Limnology & Oceanography*, 35(7), 1415–1428. https://doi.org/10.4319/lo.1990.35.7.1415
- Alldredge, A. L., & Silver, M. W. (1988). Characteristics, dynamics and significance of marine snow. *Progress in Oceanography*, 20(1), 41–82. https://doi.org/10.1016/0079-6611(88)90053-5
- Anderson, L. A., & Sarmiento, J. L. (1994). Redfield ratios of remineralization determined by nutrient data analysis. *Global Biogeochemical Cycles*, 8(1), 65–80. https://doi.org/10.1029/93gb03318
- Anderson, T. R., & Tang, K. W. (2010). Carbon cycling and POC turnover in the mesopelagic zone of the ocean: Insights from a simple model. Deep Sea Research Part II: Topical Studies in Oceanography, 57(16), 1581–1592. https://doi.org/10.1016/j.dsr2.2010.02.024
- Archibald, K. M., Siegel, D. A., & Doney, S. C. (2019). Modeling the impact of zooplankton diel vertical migration on the carbon export flux of the biological pump. *Global Biogeochemical Cycles*, 33(2), 181–199. https://doi.org/10.1029/2018gb005983
- Armstrong, R. A., Lee, C., Hedges, J. I., Honjo, S., & Wakeham, S. G. (2002). A new, mechanistic model for organic carbon fluxes in the ocean based on the quantitative association of POC with ballast minerals. *Deep Sea Research Part II: Topical Studies in Oceanography*, 49(1–3), 219–236. https://doi.org/10.1016/s0967-0645(01)00101-1
- Aumont, O., Éthé, C., Tagliabue, A., Bopp, L., & Gehlen, M. (2015). PISCES-v2: An ocean biogeochemical model for carbon and ecosystem studies. Geoscientific Model Development, 8(8), 2465–2513. https://doi.org/10.5194/gmd-8-2465-2015
- Aumont, O., Van Hulten, M., Roy-Barman, M., Dutay, J. C., Éthé, C., & Gehlen, M. (2017). Variable reactivity of particulate organic matter in a global ocean biogeochemical model. *Biogeosciences*, 14(9), 2321–2341. https://doi.org/10.5194/bg-14-2321-2017
- Basu, S., & Mackey, K. R. (2018). Phytoplankton as key mediators of the biological carbon pump: Their responses to a changing climate. Sustainability, 10(3), 869. https://doi.org/10.3390/su10030869
- Berner, R. A., & Honjo, S. (1981). Pelagic sedimentation of aragonite: Its geochemical significance. *Science*, 211(4485), 940–942. https://doi.org/10.1126/science.211.4485.940
- Bianchi, D., Dunne, J. P., Sarmiento, J. L., & Galbraith, E. D. (2012). Data-based estimates of suboxia, denitrification, and N₂O production in the ocean and their sensitivities to dissolved O., Global Bioseochemical Cycles, 26(2), GB2009, https://doi.org/10.1029/2011GB004209
- Bopp, L., Resplandy, L., Orr, J. C., Doney, S. C., Dunne, J. P., Gehlen, M., et al. (2013). Multiple stressors of ocean ecosystems in the 21st
- century: Projections with CMIP5 models. *Biogeosciences*, 10(10), 6225–6245. https://doi.org/10.5194/bg-10-6225-2013
 Boyd, P. W. (2015). Toward quantifying the response of the oceans' biological pump to climate change. *Frontiers in Marine Science*, 2(77).
- https://doi.org/10.3389/fmars.2015.00077
 Boyd, P. W., Claustre, H., Levy, M., Siegel, D. A., & Weber, T. (2019). Multi-faceted particle pumps drive carbon sequestration in the ocean.
- Nature, 568(7752), 327–335. https://doi.org/10.1038/s41586-019-1098-2
 Boyd, P. W., & Newton, P. P. (1999). Does planktonic community structure determine downward particulate organic carbon flux in different
- oceanic provinces? Deep Sea Research Part I: Oceanographic Research Papers, 46(1), 63–91. https://doi.org/10.1016/s0967-0637(98)00066-1 Boyd, P. W., Sherry, N. D., Berges, J. A., Bishop, J. K. B., Calvert, S. E., Charette, M. A., et al. (1999). Transformations of biogenic particulates from the pelagic to the deep ocean realm. Deep Sea Research Part II: Topical Studies in Oceanography, 46(11–12), 2761–2792. https://doi.org/10.1016/s0967-0645(99)00083-1
- Boyd, P. W., & Stevens, C. L. (2002). Modelling particle transformations and the downward organic carbon flux in the NE Atlantic Ocean. Progress in Oceanography, 52(1), 1–29. https://doi.org/10.1016/s0079-6611(02)00020-4
- Boyd, P. W., Strzepek, R., Fu, F., & Hutchins, D. A. (2010). Environmental control of open-ocean phytoplankton groups: Now and in the future. Limnology & Oceanography, 55(3), 1353–1376. https://doi.org/10.4319/lo.2010.55.3.1353
- Boyd, P. W., & Trull, T. W. (2007). Understanding the export of biogenic particles in oceanic waters: Is there consensus? *Progress in Oceanog-raphy*, 72(4), 276–312. https://doi.org/10.1016/j.pocean.2006.10.007
- Boyer, T. P., Garcia, H. E., Locarnini, R. A., Zweng, M. M., Mishonov, A. V., Reagan, J. R., et al. (2018). World ocean atlas 2018 [Data set]. NOAA National Centers for Environmental Information. Retrieved from https://www.ncei.noaa.gov/archive/accession/NCEI-WOA18
- Brewer, P. G., & Peltzer, E. T. (2016). Ocean chemistry, ocean warming, and emerging hypoxia: Commentary. *Journal of Geophysical Research: Oceans*, 121(5), 3659–3667. https://doi.org/10.1002/2016jc011651
- Brewer, P. G., & Peltzer, E. T. (2017). Depth perception: The need to report ocean biogeochemical rates as functions of temperature, not depth. Philosophical Transactions of the Royal Society A: Mathematical, Physical & Engineering Sciences, 375, 20160319. https://doi.org/10.1098/rsta.2016.0319
- Briggs, N., Dall'Olmo, G., & Claustre, H. (2020). Major role of particle fragmentation in regulating biological sequestration of CO₂ by the oceans. *Science*, 367(6479), 791–793. https://doi.org/10.1126/science.aay1790
- Buesseler, K. O., & Boyd, P. W. (2009). Shedding light on processes that control particle export and flux attenuation in the twilight zone of the open ocean. *Limnology & Oceanography*, 54(4), 1210–1232. https://doi.org/10.4319/lo.2009.54.4.1210
- Buesseler, K. O., Lamborg, C. H., Boyd, P. W., Lam, P. J., Trull, T. W., Bidigare, R. R., et al. (2007). Revisiting carbon flux through the ocean's twilight zone. Science, 316(5824), 567–570. https://doi.org/10.1126/science.1137959
- Buitenhuis, E. T., Le Quere, C., Bednaršek, N., & Schiebel, R. (2019). Large contribution of pteropods to shallow CaCO₃ export. Global Biogeochemical Cycles, 33(3), 458–468. https://doi.org/10.1029/2018gb006110
- Burd, A. B. (2013). Modeling particle aggregation using size class and size spectrum approaches. *Journal of Geophysical Research: Oceans*, 118(7), 3421–3443. https://doi.org/10.1002/jage.20055
- 118(7), 3431–3443. https://doi.org/10.1002/jgrc.20255
 Burd, A. B., & Jackson, G. A. (2002). Modeling steady-state particle size spectra. Environmental Science & Technology, 36(3), 323–327. https://
- doi.org/10.1021/es010982n
 Burd, A. B., & Jackson, G. A. (2009). Particle aggregation. Annual Review of Marine Science, 1, 65–90. https://doi.org/10.1146/annurev.marine.010908.163904
- Cabré, A., Marinov, I., Bernardello, R., & Bianchi, D. (2015). Oxygen minimum zones in the tropical Pacific across CMIP5 models: Mean state differences and climate change trends. *Biogeosciences*, 12(18), 5429–5454. https://doi.org/10.5194/bg-12-5429-2015
- Cavan, E. L., Trimmer, M., Shelley, F., & Sanders, R. (2017). Remineralization of particulate organic carbon in an ocean oxygen minimum zone. Nature Communications, 8(1), 1–9. https://doi.org/10.1038/ncomms14847
- Cocco, V., Joos, F., Steinacher, M., Frölicher, T. L., Bopp, L., Dunne, J., et al. (2013). Oxygen and indicators of stress for marine life in multi-model global warming projections. *Biogeosciences*, 10(3), 1849–1868. https://doi.org/10.5194/bg-10-1849-2013

DINAUER ET AL. 30 of 34



Global Biogeochemical Cycles

- 10.1029/2021GB007131
- Collins, J. R., Edwards, B. R., Thamatrakoln, K., Ossolinski, J. E., DiTullio, G. R., Bidle, K. D., et al. (2015). The multiple fates of sinking particles in the North Atlantic Ocean. *Global Biogeochemical Cycles*, 29(9), 1471–1494. https://doi.org/10.1002/2014gb005037
- Cram, J. A., Weber, T., Leung, S. W., McDonnell, A. M., Liang, J. H., & Deutsch, C. (2018). The role of particle size, ballast, temperature, and oxygen in the sinking flux to the deep sea. *Global Biogeochemical Cycles*, 32(5), 858–876. https://doi.org/10.1029/2017gb005710
- Dadou, I., Lamy, F., Rabouille, C., Ruiz-Pino, D., Andersen, V., Bianchi, M., & Garçon, V. (2001). An integrated biological pump model from the euphotic zone to the sediment: A 1-D application in the northeast tropical Atlantic. Deep Sea Research Part II: Topical Studies in Oceanography, 48(10), 2345–2381. https://doi.org/10.1016/s0967-0645(00)00177-6
- De La Rocha, C. L., Nowald, N., & Passow, U. (2008). Interactions between diatom aggregates, minerals, particulate organic carbon, and dissolved organic matter: Further implications for the ballast hypothesis. *Global Biogeochemical Cycles*, 22(4). https://doi.org/10.1029/2007GB003156
- Devol, A. H. (1978). Bacterial oxygen uptake kinetics as related to biological processes in oxygen deficient zones of the oceans. *Deep Sea Research*, 25(2), 137–146. https://doi.org/10.1016/0146-6291(78)90001-2
- Devol, A. H., & Hartnett, H. E. (2001). Role of the oxygen-deficient zone in transfer of organic carbon to the deep ocean. *Limnology & Ocean-ography*, 46(7), 1684–1690. https://doi.org/10.4319/lo.2001.46.7.1684
- DeVries, T., & Weber, T. (2017). The export and fate of organic matter in the ocean: New constraints from combining satellite and oceanographic tracer observations. *Global Biogeochemical Cycles*, 31(3), 535–555. https://doi.org/10.1002/2016gb005551
- Dilling, L., & Alldredge, A. L. (2000). Fragmentation of marine snow by swimming macrozooplankton: A new process impacting carbon cycling in the sea. *Deep Sea Research Part I: Oceanographic Research Papers*, 47(7), 1227–1245. https://doi.org/10.1016/s0967-0637(99)00105-3
- Dinauer, A. (2022a). Compiled sinking POC flux data collected by particle traps used to evaluate the MSPACMAM [Data set]. Zenodo. https://doi.org/10.5281/zenodo.6341859
- Dinauer, A. (2022b). Global 1° × 1° map of vertical POC flux profiles simulated by the MSPACMAM [Data set]. Zenodo. https://doi.org/10.5281/zenodo.6342033
- Dong, S., Berelson, W. M., Rollins, N. E., Subhas, A. V., Naviaux, J. D., Celestian, A. J., et al. (2019). Aragonite dissolution kinetics and calcite/aragonite ratios in sinking and suspended particles in the North Pacific. Earth and Planetary Science Letters, 515, 1–12. https://doi.org/10.1016/j.epsl.2019.03.016
- Ducklow, H. W., Steinberg, D. K., & Buesseler, K. O. (2001). Upper ocean carbon export and the biological pump. *Oceanography*, 14(4), 50–58. https://doi.org/10.5670/oceanog.2001.06
- Dunne, J. P., Sarmiento, J. L., & Gnanadesikan, A. (2007). A synthesis of global particle export from the surface ocean and cycling through the ocean interior and on the seafloor. *Global Biogeochemical Cycles*, 21(4). https://doi.org/10.1029/2006GB002907
- Durkin, C. A., Estapa, M. L., & Buesseler, K. O. (2015). Observations of carbon export by small sinking particles in the upper mesopelagic. Marine Chemistry, 175, 72–81. https://doi.org/10.1016/j.marchem.2015.02.011
- Engel, A., Wagner, H., Le Moigne, F. A., & Wilson, S. T. (2017). Particle export fluxes to the oxygen minimum zone of the eastern tropical North Atlantic. *Biogeosciences*, 14(7), 1825–1838. https://doi.org/10.5194/bg-14-1825-2017
- Eppley, R. W. (1972). Temperature and phytoplankton growth in the sea. Fishery Bulletin, 70(4), 1063–1085.
- Fabry, V. J. (1990). Shell growth rates of pteropod and heteropod molluscs and aragonite production in the open ocean: Implications for the marine carbonate system. *Journal of Marine Research*, 48(1), 209–222. https://doi.org/10.1357/002224090784984614
- Fay, A. R., & McKinley, G. A. (2014). Global open-ocean biomes: Mean and temporal variability. Earth System Science Data, 6(2), 273–284. https://doi.org/10.5194/essd-6-273-2014
- Francois, R., Honjo, S., Krishfield, R., & Manganini, S. (2002). Factors controlling the flux of organic carbon to the bathypelagic zone of the ocean. *Global Biogeochemical Cycles*, 16(4), 34-1–34-20. https://doi.org/10.1029/2001GB001722
- Friedrichs, M. A., Dusenberry, J. A., Anderson, L. A., Armstrong, R. A., Chai, F., Christian, J. R., et al. (2007). Assessment of skill and portability in regional marine biogeochemical models: Role of multiple planktonic groups. *Journal of Geophysical Research*, 112(C8), C08001. https://doi.org/10.1029/2006JC003852
- Gangstø, R., Gehlen, M., Schneider, B., Bopp, L., Aumont, O., & Joos, F. (2008). Modeling the marine aragonite cycle: Changes under rising carbon dioxide and its role in shallow water CaCO₃ dissolution. *Biogeosciences*, 5(4), 1057–1072. https://doi.org/10.5194/bg-5-1057-2008
- Garber, J. H. (1984). Laboratory study of nitrogen and phosphorus remineralization during the decomposition of coastal plankton and seston. Estuarine, Coastal and Shelf Science, 18(6), 685–702. https://doi.org/10.1016/0272-7714(84)90039-8
- Giering, S. L., Sanders, R., Lampitt, R. S., Anderson, T. R., Tamburini, C., Boutrif, M., et al. (2014). Reconciliation of the carbon budget in the ocean's twilight zone. *Nature*, 507(7493), 480–483. https://doi.org/10.1038/nature13123
- Gnanadesikan, A. (1999). A global model of silicon cycling: Sensitivity to eddy parameterization and dissolution. *Global Biogeochemical Cycles*, 13(1), 199–220. https://doi.org/10.1029/1998gb900013
- Goldthwait, S., Yen, J., Brown, J., & Alldredge, A. (2004). Quantification of marine snow fragmentation by swimming euphausiids. *Limnology & Oceanography*, 49(4), 940–952. https://doi.org/10.4319/lo.2004.49.4.0940
- Grill, E. V., & Richards, F. A. (1964). Nutrient regeneration from phytoplankton decomposing in seawater. *Journal of Marine Research*, 22, 51–69.
- Grossart, H. P., & Ploug, H. (2001). Microbial degradation of organic carbon and nitrogen on diatom aggregates. *Limnology & Oceanography*, 46(2), 267–277. https://doi.org/10.4319/lo.2001.46.2.0267
- Guidi, L., Stemmann, L., Jackson, G. A., Ibanez, F., Claustre, H., Legendre, L., et al. (2009). Effects of phytoplankton community on production, size, and export of large aggregates: A world-ocean analysis. *Limnology & Oceanography*, 54(6), 1951–1963. https://doi.org/10.4319/lo.2009.54.6.1951
- Hamby, D. M. (1994). A review of techniques for parameter sensitivity analysis of environmental models. Environmental Monitoring and Assessment, 32(2), 135–154. https://doi.org/10.1007/bf00547132
- Hansell, D. A., Carlson, C. A., Repeta, D. J., & Schlitzer, R. (2009). Dissolved organic matter in The ocean: A controversy stimulates new insights. Oceanography, 22(4), 202–211. https://doi.org/10.5670/oceanog.2009.109
- Henson, S. A., Sanders, R., & Madsen, E. (2012). Global patterns in efficiency of particulate organic carbon export and transfer to the deep ocean. Global Biogeochemical Cycles, 26(1). https://doi.org/10.1029/2011GB004099
- Henson, S. A., Sanders, R., Madsen, E., Morris, P. J., Le Moigne, F., & Quartly, G. D. (2011). A reduced estimate of the strength of the ocean's biological carbon pump. *Geophysical Research Letters*, 38(4). https://doi.org/10.1029/2011GL046735
- Honjo, S., & Erez, J. (1978). Dissolution rates of calcium carbonate in the deep ocean; an in situ experiment in the North Atlantic Ocean. Earth and Planetary Science Letters, 40(2), 287–300. https://doi.org/10.1016/0012-821x(78)90099-7
- Iman, R. L., & Helton, J. C. (1988). An investigation of uncertainty and sensitivity analysis techniques for computer models. Risk Analysis, 8(1), 71–90. https://doi.org/10.1111/j.1539-6924.1988.tb01155.x

DINAUER ET AL. 31 of 34



Global Biogeochemical Cycles

- 10.1029/2021GB007131
- Iversen, M. H., Nowald, N., Ploug, H., Jackson, G. A., & Fischer, G. (2010). High resolution profiles of vertical particulate organic matter export off Cape Blanc, Mauritania: Degradation processes and ballasting effects. Deep Sea Research Part I: Oceanographic Research Papers, 57(6), 771–784. https://doi.org/10.1016/j.dsr.2010.03.007
- Iversen, M. H., & Ploug, H. (2010). Ballast minerals and the sinking carbon flux in the ocean: Carbon-specific respiration rates and sinking velocity of marine snow aggregates. *Biogeosciences*, 7(9), 2613–2624. https://doi.org/10.5194/bg-7-2613-2010
- Iversen, M. H., & Ploug, H. (2013). Temperature effects on carbon-specific respiration rate and sinking velocity of diatom aggregates—potential implications for deep ocean export processes. *Biogeosciences*, 10(6), 4073–4085. https://doi.org/10.5194/bg-10-4073-2013
- Jackson, G. A. (1995). Comparing observed changes in particle size spectra with those predicted using coagulation theory. Deep Sea Research Part II: Topical Studies in Oceanography, 42(1), 159–184. https://doi.org/10.1016/0967-0645(95)00010-n
- Jackson, G. A., & Burd, A. B. (2002). A model for the distribution of particle flux in the mid-water column controlled by subsurface biotic interactions. Deep Sea Research Part II: Topical Studies in Oceanography, 49(1-3), 193-217. https://doi.org/10.1016/s0967-0645(01)00100-x
- Jackson, G. A., & Burd, A. B. (2015). Simulating aggregate dynamics in ocean biogeochemical models. Progress in Oceanography, 133, 55–265. https://doi.org/10.1016/j.pocean.2014.08.014
- Keil, R. G., Neibauer, J. A., Biladeau, C., van der Elst, K., & Devol, A. H. (2016). A multiproxy approach to understanding the "enhanced" flux of organic matter through the oxygen-deficient waters of the Arabian Sea. *Biogeosciences*, 13(7), 2077–2092. https://doi.org/10.5194/bg-13-2077-2016
- Keller, D. P., Oschlies, A., & Eby, M. (2012). A new marine ecosystem model for the University of Victoria Earth System Climate Model. Geoscientific Model Development, 5(5), 1195–1220. https://doi.org/10.5194/gmd-5-1195-2012
- Klaas, C., & Archer, D. E. (2002). Association of sinking organic matter with various types of mineral ballast in the deep sea: Implications for the rain ratio. Global Biogeochemical Cycles, 16(4), 63-1-63-14. https://doi.org/10.1029/2001GB001765
- Kostadinov, T. S., Milutinović, S., Marinov, I., & Cabré, A. (2016). Carbon-based phytoplankton size classes retrieved via ocean color estimates of the particle size distribution. Ocean Science, 12(2), 561–575. https://doi.org/10.5194/os-12-561-2016
- Kuhn, A. M., & Fennel, K. (2019). Evaluating ecosystem model complexity for the northwest North Atlantic through surrogate-based optimization. *Ocean Modelling*, 142, 101437. https://doi.org/10.1016/j.ocemod.2019.101437
- Kuhn, A. M., Fennel, K., & Berman-Frank, I. (2018). Modelling the biogeochemical effects of heterotrophic and autotrophic N₂ fixation in the Gulf of Aqaba (Israel), Red Sea. *Biogeosciences*, 15(24), 7379–7401. https://doi.org/10.5194/bg-15-7379-2018
- Kwiatkowski, L., Torres, O., Bopp, L., Aumont, O., Chamberlain, M., Christian, J. R., et al. (2020). Twenty-first century ocean warming, acidification, deoxygenation, and upper-ocean nutrient and primary production decline from CMIP6 model projections. *Biogeosciences*, 17(13), 3439–3470. https://doi.org/10.5194/bg-17-3439-2020
- Kwon, E. Y., Primeau, F., & Sarmiento, J. L. (2009). The impact of remineralization depth on the air–sea carbon balance. *Nature Geoscience*, 2(9), 630–635, https://doi.org/10.1038/ngeo612
- Lampitt, R. S., Noji, T., & Von Bodungen, B. (1990). What happens to zooplankton faecal pellets? Implications for material flux. *Marine Biology*, 104(1), 15–23. https://doi.org/10.1007/bf01313152
- Laufkötter, C., John, J. G., Stock, C. A., & Dunne, J. P. (2017). Temperature and oxygen dependence of the remineralization of organic matter. Global Biogeochemical Cycles, 31(7), 1038–1050. https://doi.org/10.1002/2017gb005643
- Laurenceau-Cornec, E. C., Trull, T. W., Davies, D. M., Christina, L., & Blain, S. (2015). Phytoplankton morphology controls on marine snow sinking velocity. Marine Ecology Progress Series, 520, 35–56. https://doi.org/10.3354/meps11116
- Laws, E. A., Falkowski, P. G., Smith, W. O., Jr., Ducklow, H., & McCarthy, J. J. (2000). Temperature effects on export production in the open ocean. Global Biogeochemical Cycles, 14(4), 1231–1246. https://doi.org/10.1029/1999gb001229
- Le Quéré, C., Buitenhuis, E. T., Moriarty, R., Alvain, S., Aumont, O., Bopp, L., et al. (2016). Role of zooplankton dynamics for Southern Ocean phytoplankton biomass and global biogeochemical cycles. *Biogeosciences*, 13(14), 4111–4133. https://doi.org/10.5194/bg-13-4111-2016
- Levitus, S. (1982). Climatological atlas of the world ocean (p. 163). U.S. Government Printing Office 13, NOAA.
- Lima, I. D., Lam, P. J., & Doney, S. C. (2014). Dynamics of particulate organic carbon flux in a global ocean model. *Biogeosciences*, 11(4), 1177–1198. https://doi.org/10.5194/bg-11-1177-2014
- Locarnini, R., Mishonov, A., Antonov, J. I., Boyer, T. P., Garcia, H., Baranova, O., et al. (2013). World Ocean atlas 2013, volume 1: Temperature. NOAA Atlas NESDIS NOAA/NESDIS, U.S. Department. of Commerce. (p. 73).
- Logan, B. E., & Wilkinson, D. B. (1990). Fractal geometry of marine snow and other biological aggregates. *Limnology & Oceanography*, 35(1), 130–136. https://doi.org/10.4319/lo.1990.35.1.0130
- Lutz, M., Dunbar, R., & Caldeira, K. (2002). Regional variability in the vertical flux of particulate organic carbon in the ocean interior. *Global Biogeochemical Cycles*, 16(3), 11-1-11-18. https://doi.org/10.1029/2000GB001383
- Maerz, J., Six, K. D., Stemmler, I., Ahmerkamp, S., & Ilyina, T. (2020). Microstructure and composition of marine aggregates as co-determinants for vertical particulate organic carbon transfer in the global ocean. *Biogeosciences*, 17(7), 1765–1803. https://doi.org/10.5194/bg-17-1765-2020
- Marsay, C. M., Sanders, R. J., Henson, S. A., Pabortsava, K., Achterberg, E. P., & Lampitt, R. S. (2015). Attenuation of sinking particulate organic carbon flux through the mesopelagic ocean. Proceedings of the National Academy of Sciences of the United States of America, 112(4), 1089–1094. https://doi.org/10.1073/pnas.1415311112
- Martin, J. H., Knauer, G. A., Karl, D. M., & Broenkow, W. W. (1987). VERTEX: Carbon cycling in the northeast Pacific. *Deep Sea Research Part A. Oceanographic Research Papers*, 34(2), 267–285. https://doi.org/10.1016/0198-0149(87)90086-0
- Matsumoto, K. (2007). Biology-mediated temperature control on atmospheric pCO₂ and ocean biogeochemistry. Geophysical Research Letters, 34(20), L20605. https://doi.org/10.1029/2007GL031301
- Matsumoto, K., Hashioka, T., & Yamanaka, Y. (2007). Effect of temperature-dependent organic carbon decay on atmospheric pCO₂. Journal of Geophysical Research, 112(G2), G02007. https://doi.org/10.1029/2006JG000187
- McDonnell, A. M., & Buesseler, K. O. (2010). Variability in the average sinking velocity of marine particles. *Limnology & Oceanography*, 55(5), 2085–2096. https://doi.org/10.4319/lo.2010.55.5.2085
- McDonnell, A. M. P., Boyd, P. W., & Buesseler, K. O. (2015). Effects of sinking velocities and microbial respiration rates on the attenuation of particulate carbon fluxes through the mesopelagic zone. Global Biogeochemical Cycles, 29(2), 175–193. https://doi.org/10.1002/2014gb004935
- McDougall, T. J., & Barker, P. M. (2011). Getting started with TEOS-10 and the Gibbs Seawater (GSW) oceanographic Toolbox, SCOR/IAPSO WG127, ISBN 978-0-646-55621-5.
- Najjar, R. G., Jin, X., Louanchi, F., Aumont, O., Caldeira, K., Doney, S. C., et al. (2007). Impact of circulation on export production, dissolved organic matter, and dissolved oxygen in the ocean: Results from phase II of the ocean carbon-cycle Model intercomparison project (OCMIP-2). Global Biogeochemical Cycles, 21(3), GB3007. https://doi.org/10.1029/2006GB002857
- Naviaux, J. D., Subhas, A. V., Dong, S., Rollins, N. E., Liu, X., Byrne, R. H., et al. (2019). Calcite dissolution rates in seawater: Lab vs. in situ measurements and inhibition by organic matter. *Marine Chemistry*, 215, 103684. https://doi.org/10.1016/j.marchem.2019.103684

DINAUER ET AL. 32 of 34

- Nayar, K. G., Sharqawy, M. H., Banchik, L. D., & Lienhard, J. H. (2016). Thermophysical properties of seawater: A review and new correlations that include pressure dependence. *Desalination*, 390, 1–24. https://doi.org/10.1016/j.desal.2016.02.024
- Olsen, A., Key, R. M., Van Heuven, S., Lauvset, S. K., Velo, A., Lin, X., et al. (2016). The Global Ocean Data Analysis Project version 2 (GLODAPv2) an internally consistent data product for the world ocean. *Earth System Science Data*, 8, 297–323. https://doi.org/10.5194/essd-8-297-2016
- Omand, M. M., Govindarajan, R., He, J., & Mahadevan, A. (2020). Sinking flux of particulate organic matter in the oceans: Sensitivity to particle characteristics. Scientific Reports, 10(1), 1–16. https://doi.org/10.1038/s41598-020-60424-5
- Owens, S. A., Buesseler, K. O., Lamborg, C. H., Valdes, J., Lomas, M. W., Johnson, R. J., et al. (2013). A new time series of particle export from neutrally buoyant sediments traps at the Bermuda Atlantic Time-series study site. *Deep Sea Research Part I: Oceanographic Research Papers*, 72, 34–47. https://doi.org/10.1016/j.dsr.2012.10.011
- Passow, U., & Carlson, C. A. (2012). The biological pump in a high CO₂ world. Marine Ecology Progress Series, 470, 249–271. https://doi.org/10.3354/meps09985
- Passow, U., & De La Rocha, C. L. (2006). Accumulation of mineral ballast on organic aggregates. Global Biogeochemical Cycles, 20(1). https://doi.org/10.1029/2005GB002579
- Pianosi, F., Beven, K., Freer, J., Hall, J. W., Rougier, J., Stephenson, D. B., & Wagener, T. (2016). Sensitivity analysis of environmental models: A systematic review with practical workflow. *Environmental Modelling & Software*, 79, 214–232. https://doi.org/10.1016/j.envsoft.2016.02.008
- Ploug, H., & Grossart, H. P. (2000). Bacterial growth and grazing on diatom aggregates: Respiratory carbon turnover as a function of aggregate size and sinking velocity. Limnology & Oceanography, 45(7), 1467–1475. https://doi.org/10.4319/lo.2000.45.7.1467
- Ploug, H., Grossart, H. P., Azam, F., & Jørgensen, B. B. (1999). Photosynthesis, respiration, and carbon turnover in sinking marine snow from surface waters of Southern California Bight: Implications for the carbon cycle in the ocean. Marine Ecology Progress Series, 179, 1–11. https://doi.org/10.3354/meps179001
- Ploug, H., Iversen, M. H., & Fischer, G. (2008). Ballast, sinking velocity, and apparent diffusivity within marine snow and zooplankton fecal pellets: Implications for substrate turnover by attached bacteria. *Limnology & Oceanography*, 53(5), 1878–1886. https://doi.org/10.4319/
- Ploug, H., Iversen, M. H., Koski, M., & Buitenhuis, E. T. (2008). Production, oxygen respiration rates, and sinking velocity of copepod fecal pellets: Direct measurements of ballasting by opal and calcite. *Limnology & Oceanography*, 53(2), 469–476. https://doi.org/10.4319/10.2008.53.2.0469
- Primeau, F. (2005). Characterizing transport between the surface mixed layer and the ocean interior with a forward and adjoint global ocean transport model. *Journal of Physical Oceanography*, 35(4), 545–564. https://doi.org/10.1175/jpo2699.1
- Resplandy, L., Lévy, M., & McGillicuddy, D. J., Jr. (2019). Effects of eddy-driven subduction on ocean biological carbon pump. Global Biogeochemical Cycles. 33(8), 1071–1084. https://doi.org/10.1029/2018gb006125
- Richardson, T. L. (2019). Mechanisms and pathways of small-phytoplankton export from the surface ocean. *Annual Review of Marine Science*, 11(1), 57–74. https://doi.org/10.1146/annurev-marine-121916-063627
- Roth, R., Ritz, S. P., & Joos, F. (2014). Burial-nutrient feedbacks amplify the sensitivity of atmospheric carbon dioxide to changes in organic matter remineralisation. *Earth System Dynamics*, 5(2), 321–343. https://doi.org/10.5194/esd-5-321-2014
- Rubey, W. W. (1933). Settling velocities of gravel, sand, and silt particles. American Journal of Science, s5-25(148), 325–338. https://doi.org/10.2475/ais.s5-25.148.325
- Sarmiento, J. L., & Gruber, N. (2006). Ocean biogeochemical dynamics. Princeton University Press.
- Segschneider, J., & Bendtsen, J. (2013). Temperature-dependent remineralization in a warming ocean increases surface pCO₂ through changes in marine ecosystem composition. Global Biogeochemical Cycles, 27(4), 1214–1225. https://doi.org/10.1002/2013gb004684
- Seiki, T., Date, E., & Izawa, H. (1991). Decomposition characteristics of particulate organic matter in Hiroshima Bay. *Journal of the Oceano-graphical Society of Japan*, 47(5), 207–220. https://doi.org/10.1007/bf02310036
- Sharqawy, M. H., Lienhard, J. H., & Zubair, S. M. (2010). Thermophysical properties of seawater: A review of existing correlations and data. Desalination and Water Treatment, 16(1–3), 354–380. https://doi.org/10.5004/dwt.2010.1079
- Siegel, D. A., Buesseler, K. O., Behrenfeld, M. J., Benitez-Nelson, C. R., Boss, E., Brzezinski, M. A., et al. (2016). Prediction of the export and fate of global ocean net primary production: The EXPORTS science plan. Frontiers in Marine Science, 3(22). https://doi.org/10.3389/fmars.2016.00022
- Siegel, D. A., Buesseler, K. O., Doney, S. C., Sailley, S. F., Behrenfeld, M. J., & Boyd, P. W. (2014). Global assessment of ocean carbon export by combining satellite observations and food-web models. *Global Biogeochemical Cycles*, 28(3), 181–196. https://doi.org/10.1002/2013gb004743
- Sonnerup, R. E., Mecking, S., & Bullister, J. L. (2013). Transit time distributions and oxygen utilization rates in the Northeast Pacific Ocean from chlorofluorocarbons and sulfur hexafluoride. *Deep Sea Research Part I: Oceanographic Research Papers*, 72, 61–71. https://doi.org/10.1016/j. dsr.2012.10.013
- Sonnerup, R. E., Mecking, S., Bullister, J. L., & Warner, M. J. (2015). Transit time distributions and oxygen utilization rates from chlorofluor-ocarbons and sulfur hexafluoride in the Southeast Pacific Ocean. *Journal of Geophysical Research: Oceans*, 120(5), 3761–3776. https://doi.org/10.1002/2015jc010781
- Stanley, R. H., Doney, S. C., Jenkins, W. J., & Lott, D. E., III. (2012). Apparent oxygen utilization rates calculated from tritium and helium-3 profiles at the Bermuda Atlantic Time-series study site. *Biogeosciences*, 9(6), 1969–1983. https://doi.org/10.5194/bg-9-1969-2012
- Steinberg, D. K., Van Mooy, B. A., Buesseler, K. O., Boyd, P. W., Kobari, T., & Karl, D. M. (2008). Bacterial vs. zooplankton control of sinking particle flux in the ocean's twilight zone. *Limnology & Oceanography*, 53(4), 1327–1338. https://doi.org/10.4319/lo.2008.53.4.1327
- Stemmann, L., Jackson, G. A., & Ianson, D. (2004). A vertical model of particle size distributions and fluxes in the midwater column that includes biological and physical processes—Part I: Model formulation. *Deep Sea Research Part I: Oceanographic Research Papers*, 51(7), 865–884. https://doi.org/10.1016/j.dsr.2004.03.001
- Stokes, G. G. (1851). On the effect of the internal friction of fluids on the motion of pendulums. Transactions of the Cambridge Philosophical Society, 9(2), 8–106.
- Stow, C. A., Jolliff, J., McGillicuddy, D. J., Jr., Doney, S. C., Allen, J. I., Friedrichs, M. A., et al. (2009). Skill assessment for coupled biological/physical models of marine systems. *Journal of Marine Systems*, 76(1–2), 4–15. https://doi.org/10.1016/j.jmarsys.2008.03.011
- Subhas, A. V., Rollins, N. E., Berelson, W. M., Erez, J., Ziveri, P., Langer, G., & Adkins, J. F. (2018). The dissolution behavior of biogenic calcites in seawater and a possible role for magnesium and organic carbon. *Marine Chemistry*, 205, 100–112. https://doi.org/10.1016/j.
- Taucher, J., Bach, L. T., Riebesell, U., & Oschlies, A. (2014). The viscosity effect on marine particle flux: A climate relevant feedback mechanism. Global Biogeochemical Cycles, 28(4), 415–422. https://doi.org/10.1002/2013gb004728

DINAUER ET AL. 33 of 34

- Thamdrup, B., & Fleischer, S. (1998). Temperature dependence of oxygen respiration, nitrogen mineralization, and nitrification in Arctic sediments. *Aquatic Microbial Ecology*, 15(2), 191–199. https://doi.org/10.3354/ame015191
- Turner, J. T. (2002). Zooplankton fecal pellets, marine snow and sinking phytoplankton blooms. Aquatic Microbial Ecology, 27(1), 57–102. https://doi.org/10.3354/ame027057
- Turner, J. T. (2015). Zooplankton fecal pellets, marine snow, phytodetritus and the ocean's biological pump. *Progress in Oceanography*, 130, 205–248. https://doi.org/10.1016/j.pocean.2014.08.005
- Van Mooy, B. A., Keil, R. G., & Devol, A. H. (2002). Impact of suboxia on sinking particulate organic carbon: Enhanced carbon flux and preferential degradation of amino acids via denitrification. Geochimica et Cosmochimica Acta, 66(3), 457–465. https://doi.org/10.1016/s0016-7037(01)00787-6
- Volk, T., & Hoffert, M. I. (1985). Ocean carbon pumps: Analysis of relative strengths and efficiencies in ocean-driven atmospheric CO₂ changes. The Carbon Cycle and Atmospheric CO₂: Natural Variations Archean to Present, 32, 99–110.
- Weber, T., & Bianchi, D. (2020). Efficient particle transfer to depth in oxygen minimum zones of the Pacific and Indian Oceans. Frontiers of Earth Science, 8(376). https://doi.org/10.3389/feart.2020.00376
- Weber, T., Cram, J. A., Leung, S. W., DeVries, T., & Deutsch, C. (2016). Deep ocean nutrients imply large latitudinal variation in particle transfer efficiency. Proceedings of the National Academy of Sciences of the United States of America, 113(31), 8606–8611. https://doi.org/10.1073/ pnas.1604414113
- Westrich, J. T., & Berner, R. A. (1984). The role of sedimentary organic matter in bacterial sulfate reduction: The G model tested 1. Limnology & Oceanography, 29(2), 236–249. https://doi.org/10.4319/lo.1984.29.2.0236
- White, P. A., Kalff, J., Rasmussen, J. B., & Gasol, J. M. (1991). The effect of temperature and algal biomass on bacterial production and specific growth rate in freshwater and marine habitats. *Microbial Ecology*, 21(1), 99–118. https://doi.org/10.1007/bf02539147
- Xiao, Y., & Friedrichs, M. A. (2014). The assimilation of satellite-derived data into a one-dimensional lower trophic level marine ecosystem model. *Journal of Geophysical Research: Oceans*, 119(4), 2691–2712. https://doi.org/10.1002/2013jc009433
- Yool, A., Popova, E. E., & Anderson, T. R. (2013). MEDUSA-2.0: An intermediate complexity biogeochemical model of the marine carbon cycle for climate change and ocean acidification studies. *Geoscientific Model Development*, 6(5), 1767–1811. https://doi.org/10.5194/gmd-6-1767-2013

DINAUER ET AL. 34 of 34